

UCLA

UCLA Electronic Theses and Dissertations

Title

Investigations of Point Defect Properties and Dislocation Mechanisms in the Equiatomic Nb-Mo-Ta-W Refractory Alloy by Computational Modeling and Simulations

Permalink

<https://escholarship.org/uc/item/8kd8x3mp>

Author

Zhou, Xinran

Publication Date

2024

Peer reviewed|Thesis/dissertation

UNIVERSITY OF CALIFORNIA

Los Angeles

Investigations of Point Defect Properties and Dislocation Mechanisms in the
Equiatomic Nb-Mo-Ta-W Refractory Alloy by Computational Modeling and Simulations

A dissertation submitted in partial satisfaction
of the requirements for the degree
Doctor of Philosophy in Materials Science and Engineering

by

Xinran Zhou

2024

© Copyright by

Xinran Zhou

2024

ABSTRACT OF THE DISSERTATION

Investigations of Point Defect Properties and Dislocation Mechanisms in the
Equiatomic Nb-Mo-Ta-W Refractory Alloy by Computational Modeling and Simulations

by

Xinran Zhou

Doctor of Philosophy in Materials Science and Engineering

University of California, Los Angeles, 2024

Professor Jaime Marian, Chair

Refractory multi-element alloys (RMEA) with body-centered cubic (bcc) structure have been the object of much research over the last decade due to their high potential as candidate structural materials for applications in harsh environments such as power plants, aerospace industry, or nuclear sectors. However, theories are yet to be developed to fully explain their exceptional strength at elevated temperatures, as well as to either verify or refute whether they are as irradiation-tolerant as they are considered to be. A good starting point to dig in is that macroscopic irradiation behavior of the alloys is known to be connected with properties at atomic-level through the roles of point defects, i.e., self-interstitial atoms (SIA) and vacancies. As for high-temperature strength, it is hypothesized that global chemical fluctuations in these complex alloys are major causes of strengthening through interactions with screw dislocation that significantly alter dislocation energetics and mechanisms which are known to control the plasticity of classical bcc metals and dilute alloys.

Among all members of the RMEA family, the equiatomic Nb-Mo-Ta-W system has become a model alloy of the RMEA group due to its phase stability, microstructural simplicity,

and mixture of elements with high lattice distortion, making it an ideal experimental and computational test bed to study fundamental behavior. Therefore, to explore the above points and implement the modern theories, we use atomistic simulations to study the properties vacancies as well as self-interstitial atoms in the quaternary equiatomic Nb-Mo-Ta-W refractory alloy. To investigate the bcc RMEA plasticity, we develop a kinetic Monte Carlo (kMC) model to simulate screw dislocation motion in RMEAs and perform simulations to study the relationship between dislocation mechanisms and alloy strength and quantify the contribution to the total strength due to screw dislocation.

In our investigation of vacancy properties in Nb-Mo-Ta-W, we calculate their energetics in the equiatomic Nb-Mo-Ta-W alloy, especially vacancy formation and migration energies, using molecular statics calculations based on a spectral neighbor analysis potential specifically developed for Nb-Mo-Ta-W. We consider vacancy properties in bulk environments including the effect of short-range order (SRO) by preparing supercells through Metropolis Monte-Carlo relaxations, and temperature on the calculation. The nudged elastic band (NEB) method is applied to study vacancy migration energies. Our results show that both vacancy formation energies and vacancy migration energies are statistically distributed with a wide spread, on the order of 1.0 eV in some cases, and display a noticeable dependence on SRO. Moreover, the large spread in vacancy formation energies results in an asymmetric thermal sampling of the formation energy distribution towards lower values. This gives rise to *effective* vacancy formation energies that are noticeably lower than the distribution averages. We study the effect that this phenomenon has on the vacancy diffusivity in the alloy and discuss the implications of our findings on the structural features of Nb-Mo-Ta-W.

In our study of SIA properties in Nb-Mo-Ta-W, it is found that the $\langle 111 \rangle$ orientation to be the most common among all split configurations. Chemically, these SIA defects adopt a variety of structures involving all pairs of atoms, including –surprisingly– a relatively high occurrence of octahedral SIA. In terms of their diffusivities, we find two clearly distinguished regimes at and below 600 K and above it, where the SIA diffusion changes dimensionality

from 1D to 3D. We calculate the migration energies and diffusion pre-factors in both regions, from which we extract the translational and rotational components of the defect migration. We find values of 0.25 eV and pre-factors of $\sim 10^{-11} \text{ m}^2 \cdot \text{s}^{-1}$ in the low temperature regime, and 0.57 eV and $\sim 10^{-8} \text{ m}^2 \cdot \text{s}^{-1}$ in the high temperature one, and estimate the rotational energy barrier at 0.37 eV.

Our simulations of screw dislocation kinetics indicate, in agreement with molecular dynamics simulations, that chemical energy fluctuations along the dislocation line lead to measurable concentrations of kinks in equilibrium in a wide temperature range. A fraction of these form cross-kink configurations, which are ultimately found to control screw dislocation motion and material strength. It is found that the self-pinning stress remains even at high temperatures due to the balance of two competing effects: strengthening due to higher concentrations of kinks on multiple glide planes, and softening associated with the thermal dissolution of cross-kinks.

The dissertation of Xinran Zhou is approved.

Gregory P. Carman

Amartya S. Banerjee

Qibing Pei

Jaime Marian, Committee Chair

University of California, Los Angeles

2024

TABLE OF CONTENTS

1 Vacancy Energetics and Diffusive Properties in the Equiatomic Nb-Mo-Ta-W Alloy	1
1.1 Introduction	1
1.2 Methods	3
1.2.1 Molecular statics calculations	3
1.2.2 Metropolis Monte-Carlo Method	4
1.2.3 Vacancy formation and migration energies	4
1.3 Results	5
1.3.1 Equilibrium lattice parameter	5
1.3.2 Short range order calculation	7
1.3.3 Vacancy energetics in bulk systems	10
1.3.4 Vacancy energetics at edge dislocation cores	16
1.4 Discussion	18
1.4.1 Statistical distribution of vacancy energetics	18
1.4.2 Analysis of vacancy formation energy and migration energy	18
1.4.3 Self-diffusion coefficients of Nb-Mo-Ta-W	21
1.4.4 Comparison with other works	23
1.5 Conclusions	25
2 Self-interstitial Configurations, Energetics and Diffusive Properties in the Equiatomic Nb-Mo-Ta-W Alloy	27
2.1 Introduction	27

2.2	Methods	29
2.2.1	Atomistic calculations	29
2.2.2	Defect energy calculations	30
2.3	Results	32
2.3.1	Formation energies of self-interstitial atoms	32
2.3.2	Diffusion of self-interstitial atoms in Nb-Mo-Ta-W	36
2.4	Discussion	41
2.5	Conclusions	43
3	Kinetic Monte Carlo (kMC) Modeling of Screw Dislocation Motions in the Equimolar Nb-Mo-Ta-W Alloys	45
3.1	Introduction	45
3.2	Methodology	46
3.3	Results	48
3.3.1	Stress-free dislocation line relaxations	48
3.3.2	Velocity-stress relations	52
3.3.3	Temperature dependence of the dislocation critical stress	55
3.4	Discussion	56
3.5	Conclusions	58

LIST OF FIGURES

1.1	Potential energy per atom as a function of a for random equiatomic Nb-Mo-Ta-W.	6
1.2	Energy evolution of the random Nb-Mo-Ta-W during annealing at different temperatures. The total energy of the system at the initial state is zero for easier reference.	8
1.3	1NN Warren Cowley parameter as a function of annealing temperature.	9
1.4	The distributions of vacancy formation energies of: (a-e) cells with SRO (annealing temperature from 300 K to 1500 K) and (f) the random cell of Nb-Mo-Ta-W. The dashed line shows the position of the statistical average of each distribution.	11
1.5	Effective vacancy formation energy as a function of temperature. The horizontal line represents the statistical average in the vacancy formation energy distribution of the random Nb-Mo-Ta-W bulk. The shadow region highlights the difference between effective energies and the statistical average value.	14
1.6	The MEPs of vacancy migration in (a) pure constituent metals and (b) the equiatomic random Nb-Mo-Ta-W.	15
1.7	The distributions of vacancy migration energies of: (a-e) cells with SRO (annealing temperature from 300 K to 1500 K) and (f) the random cell of Nb-Mo-Ta-W. The dashed line shows the position of the statistical average of each distribution.	16
1.8	The distributions of vacancy migration energies when: (a) only one [111] direction is considered and (b) all eight directions of [111] type are considered.	18
1.9	A cell of random Nb-Mo-Ta-W with an edge dislocation dipole. The ‘ \perp ’ symbols mark the exact locations of dislocation cores. The dashed circles indicate locations with varying atomic distances from dislocation cores (e.g. position ‘0’ is of zero interatomic distance from the core). Colors represent different atomic species: red = Ta, blue = Nb, yellow = Mo, green = W.	19

1.10	Vacancy formation energies as a function of distance from the edge dislocation core. The labeled positions in the x axis refer to the locations shown in Figure 1.9. The point labeled as 'random bulk' gives the formation energy obtained in Section 1.3.3.	20
1.11	Diffusivities of Nb-Mo-Ta-W and its pure constituents as a function of temperature.	24
2.1	Split dumbbell configurations in BCC crystals: (a) $\langle 110 \rangle$ orientation, (b) $\langle 111 \rangle$ orientation, and (c) $\langle 001 \rangle$ orientation. (d) and (e), tetrahedral and octahedral configurations. The atom colored in black represents the extra atom that forms the self-interstitial configuration.	32
2.2	Normalized histograms of the final configurations observed in random Nb-Mo-Ta-W alloys for insertions of the same type of atomic species (indicated under each subfigure). Note that insertion of an extra atom of species α does not necessarily have to lead to an self-interstitial containing that same species.	34
2.3	Relative occurrence of each type of SIA structure observed after relaxation. . . .	35
2.4	Violin plot showing the SIA formation energies in random Nb-Mo-Ta-W alloys for all structures observed. Octahedral configurations are placed on the left (no 'oct-Ta' structures were stable), followed by the energies of the $\langle 100 \rangle$, $\langle 110 \rangle$, and $\langle 111 \rangle$ configurations for split SIA pairs. 'SD' stands for "standard deviation" (in the legend).	36
2.5	Spatial trajectories of SIA defects at different temperatures in equiatomic Nb-Mo-Ta-W alloys.	38
2.6	Evolution with time of the diffusivity of self-interstitial atoms at several temperatures. Dashed lines indicate asymptotic fits at each temperature.	38
2.7	SIA diffusivities as a function of inverse temperature. Orange and blue dashed lines are fits to eq. (2.7) separating the 1D and 3D diffusing temperature regions.	39

3.1	(a) View of the dislocation core along the [111] direction showing the minimal atomic environment needed to capture all kink-pair nucleation events. The dashed polygons represent the maximum extent of dislocation-atom interactions. (b) Spread of a single kink along the [111] direction indicating the region over which the interaction energy is calculated. For clarity, only atoms immediately surrounding the two adjacent Peierls valleys are shown. The inset to the figure shows the variation of $\Delta E_{y \rightarrow y+b}^{int}$ along a path of length $70b$ to showcase the rough chemical energy landscape encountered by kinks during their motion.	50
3.2	(a) Dislocation configuration after thermalization at 900 K. Kinks and cross-kinks emerge spontaneously during equilibration on all available {110} planes. (b) Line configuration after 1 μs of dislocation motion under 800 MPa of applied stress. Screw segments are colored in gray. All other segments are color-coded according to their glide plane. The size marker is common to both images	51
3.3	Equilibrium concentration of kink pairs and cross-kinks per unit length in Burgers vector units as a function of (inverse) temperature. Two regimes can be clearly appreciated, each characterized by Arrhenius fits with energies of 0.003 and 0.016 eV at low and high temperatures, respectively. Orange dots represent the equilibrium concentration of cross-kinks as a function of T . Error bars are representative of the standard variation obtained from 10 independent simulations at each temperature.	51
3.4	Mean screw dislocation velocity as a function of resolved shear stress and temperature for $500b$ dislocation lines. Dashed lines represent best fits to power laws of the type: $v(\tau) = a(\tau - \tau_{s-p})^m$. Open circles correspond to simulations in pure W under the same conditions at 300 and 900 K. Pure W simulations follow a perfect exponential velocity-stress dependence, with no threshold stress at any temperature. The orange curve corresponds to the ‘average’ Nb-Mo-Ta-W alloy at 600 K.	53

3.5 Temperature dependence of the critical stress for screw dislocation motion. The total stress results from the additive effects of the thermal stress (due to thermally-activated processes), and the self-pinning stress (due to the intrinsic line roughness under zero applied stress conditions). Black dots correspond to MD results of the critical (threshold) stress from ref. [1]. 55

LIST OF TABLES

1.1	Simulated equilibrium lattice parameters of the random equiatomic Nb-Mo-Ta-W alloy, the 'average' alloy and the individual constituents metals.	7
1.2	The chemical potential energies of pure elements and the average alloy computed in the context of the pure metals. The 'average' represents the weighted average of chemical potential energies of Nb,Ta,Mo and W.	10
1.3	Statistical averages of vacancy formation energy distributions of Nb-Mo-Ta-W and vacancy formation energies of the pure constituents. The 'average' represents the weighted average of vacancy formation energies of Nb,Ta,Mo and W.	12
1.4	The effective vacancy formation energies of Nb-Mo-Ta-W at different temperatures.	13
1.5	Statistical averages of vacancy migration energy distributions of Nb-Mo-Ta-W and vacancy migration energies of the pure constituents. The 'average' represents the weighted average of vacancy migration energies of Nb,Ta,Mo and W.	17
1.6	Statistical averages of vacancy formation energy distributions of position '0' in alloys with varying degrees of SRO. The 'average' represents the weighted average of vacancy formation energies at position '0' in Nb,Ta,Mo and W.	21
1.7	Parameters and pre-exponential factors used in calculation of diffusivity.	23
2.1	Calculated chemical potentials for the equiatomic Nb-Mo-Ta-W alloy and the pure elements. The results for the alloy were extracted from 130 independent alloy configurations in supercells containing 24192 atoms. The last two columns give the lattice parameters of the pure elements and the lattice distortion relative to pure W: $\delta = (a_0^\alpha - a_0^W) / a_0^W$	31

2.2	SIA formation energies for the $\langle 111 \rangle$ configurations in the elemental metals calculated in this work using the SNAP potential (in bold text), and published in other works. ‘DFT’: density functional theory. ‘BOP’: bond-order potentials. All energies are in eV.	33
2.3	Diffusion parameters extracted from Fig. 2.7.	40
2.4	Pre-exponential factors and SIA migration energies found in the literature for the pure elements Nb, Mo, Ta, and W.	40
3.1	Parameters needed for eqs. (3.1)-(3.3). The values for ΔH_0 and τ_P are obtained as weighted averages of the pure element values as calculated in ref. [2]. The image in the rightmost column shows the relaxed structure of a screw dislocation dipole in the random solid solution (only the dislocation lines are depicted). The length of the lines is equal to $80b$. Several kink pairs can be seen to emerge in the ground state of the dislocation lines.	49
3.2	Parameters of the power fits shown in Figure 3.4 according to eq. 3.4.	54

ACKNOWLEDGMENTS

I would like to express my sincere gratitude to my faculty advisor, Prof. Jaime Marian, for his invaluable guidance and support over the past five years. His professional expertise and mentorship have been instrumental in not only my academic advancement but also personal growth.

I would also like to send my thankful regards to my mentor, Dr. Vasily V. Bulatov for his invaluable supervision in our collaboration project. He's such a insightful and energetic scientist with full of ideas, who have inspired and encouraged me significantly.

I would like to appreciate Prof. Qibing Pei and Dr. Fei Zhou, for their thoughtful advice and generous help they provided during the academic years. In addition, please allow me to thank my colleagues and collaborators who are willing to give their kind supports.

I would like to thank my parents for their unconditional support and encouragement throughout my academic journey. Your love is my strength.

At last, thank you all for contributing to my PhD program. It's a wonderful journey with all of you, which I shall always remember.

VITA

- 2018 B.S., Materials Science and Engineering Department, Shanghai University.
- 2021 Winter Teaching Assistant, Materials Science and Engineering Department, UCLA. Taught sections of MAT 143A (beginning materials mechanical property course) under direction of Professor Jaime Marian.
- 2023 Summer CCMS Internship, Materials Science Division, LLNL.
- 2020–2024 Graduate Student Researcher, Materials Science and Engineering Department, UCLA.

PUBLICATIONS

- Zhou, X., He, S., & Marian, J. (2021). Cross-kinks control screw dislocation strength in equiatomic bcc refractory alloys. *Acta Materialia*, 211, 116875.
- Zhou, X., He, S., & Marian, J. (2024). Temperature Dependence of the Strength of Nb-Mo-Ta-W Alloys Due to Screw Dislocations. *Scripta Materialia*, 239, 115815
- Zhou, X., Wang, X., Fey, L., He, S., Beyerlein, I., Cao, P., & Marian, J. (2023). Models of dislocation glide and strengthening mechanisms in bcc complex concentrated alloys. *MRS Bulletin*, 48(7), 777-789
- Zhou, X., Barnett, A., Hopkins, E., Falk, M., Taheri M., & Marian, J. Self-interstitial atom properties in Nb-Mo-Ta-W alloys. *Computational Materials Science*, 234, 112765

Zhou, X., He, S., & Marian, J. (2022). Vacancy energetics and diffusivities in the equiatomic multielement nb-mo-ta-w alloy. *Materials*, 15(15), 5468

Zhou, X., & Marian, J. (2021). Temperature and stress dependence of screw dislocation mobility in nb-v-ta alloys using kinetic montecarlo simulations. *Frontiers in Materials*, 8, 801141

He, S., Zhou, X., Mordehai, D., & Marian, J. (2023). Thermal super-jogs control the high-temperature strength plateau in Nb-Mo-Ta-W alloys. *Acta Materialia*, 244, 118539

Zhao, Y., Dezerald, L., Pozuelo, M., Zhou, X., & Marian, J. (2020). Simulating the mechanisms of serrated flow in interstitial alloys with atomic resolution over diffusive timescales. *Nature communications*, 11(1), 1227

Jacobs, M., Zhou, X., Olivera, E., Sheil, R., Huang, S., Marszewski, M., ... & Marian, J. (2021). Room temperature rectification in tapered-channel thermal diodes through nanoscale confinement-induced liquid–solid phase change. *Journal of Applied Physics*, 129(7)

Wu, X. T., Xu, Z. F., Zhou, X. R., Wang, H., & Lu, X. G. (2019). Reinvestigation of the Bulk Modulus for fcc Al using a Helmholtz Energy Approach. *International Journal of Thermophysics*, 40, 1-15

CHAPTER 1

Vacancy Energetics and Diffusive Properties in the Equiatomic Nb-Mo-Ta-W Alloy

1.1 Introduction

High-entropy alloys (HEA), also known as multicomponent alloy or multiprincipal element alloys consist of four or more distinct elements in equimolar or near equimolar proportions [3–7]. Some HEA are observed to exhibit combinations of desirable properties which are not common in conventional alloys such as good irradiation resistance, corrosion resistance, thermal stability, and high strength [8–10], especially under harsh working environments. This makes them attractive candidate materials for applications in the energy sector, the aerospace industry, and transportation industries [11–14]. Their extraordinary properties and great potential for a variety of applications have stimulated research to investigate the underlying mechanisms [15–20]. Among the several different classes of HEA [9], refractory multi-element alloys (RMEA) are composed of up to four or more refractory transition metals from group IVB, VB, VIB [16, 21]. As its name indicates, RMEAs are attractive for their outstanding mechanical properties at elevated temperatures. They are able to retain a single phase bcc structure and have well-balanced combinations of high strength-weight ratio, fracture toughness and ductility up to very high temperatures [22–27]. It is thought that the limited self-diffusion reported for most RMEA plays a key role in the outstanding thermal stability and mechanical properties at high temperatures.

At high temperatures, vacancy properties are known to control RMEA performance such

as the irradiation resistance, phase stability and creep deformation [28–31]. Thus, gaining a detailed understanding of vacancy energetics is a first important step to quantify the parameters that govern mass transport properties in these alloys. Of particular interest is the quantification of the (self) diffusion coefficient, which is universally reported to be very low for RMEA such as Nb-Mo-Ta-W [32–34]. As well, it is important to study the implications of high configurational entropy on defect properties such as those of vacancies, both structurally and also in terms of the statistical significance of having a large spread in the energy distributions.

For example, many works have shown that short-range order (SRO) can have significantly effects on the mechanical, electronic, magnetic and irradiation properties of HEAs [35–40], as well as vacancy energetics [41–43]. Thus, to gain a more comprehensive understanding of the interactions between chemical lattice complexity and vacancy energetics in HEAs, an investigation into the effect of SRO on vacancy energetics is of the essence.

Further, with vacancy formation energies in RMEA presumed to be as high as in the pure elemental refractory elements, it is expected that heterogeneous nucleation at intrinsic defects such as dislocations and grain boundaries will be the dominant source of vacancies [43, 44]. Thus, here we also consider vacancy energetics in the proximity of edge dislocation cores.

While it is well known that refractory metals display high vacancy formation energies, in multi-principal element alloys bulk formation energies are often distributed across a wide energy range [45–48]. This introduces the possibility of energies significantly lower than the distribution averages [45, 46], opening the door to enhanced vacancy-mediated behavior compared to pure refractory metals. Moreover, since vacancies are generally produced at material heterogeneities, it is of interest to investigate the differences between formation energy distributions in the bulk and at selected material defects such as dislocations, grain boundaries, and free surfaces. While bulk vacancy formation distributions have been calculated for selected refractory multi-principal element alloys [48–50], here we also investigate

vacancy formation at edge dislocation cores and study the implications on diffusion and dislocation climb of broadly-distributed vacancy energies in Nb-Mo-Ta-W. As well, we study vacancy migration in the bulk and at the edge dislocation core to understand the effect that chemical composition has on these properties. To our knowledge, this has not been done before.

The chapter is organized as follows. First, we discuss the atomistic simulation method, including the details of construction of the random Nb-Mo-Ta-W model, the construction of supercells with SRO, and the methods of calculating vacancy formation and migration energies, E_V^f and E_V^m , in a variety of scenarios. Then, we present results for E_V^f and E_V^m as a function of temperature by adopting supercell constrictions with the appropriate SRO at each temperature. As well, we report on the results of the same calculations but in the presence of an edge dislocation. This is followed by a discussion to provide detailed analysis of the results and demonstrate how the results may be used to calculate the diffusion coefficient in the alloy. Finally, we end the chapter with our main conclusions.

1.2 Methods

1.2.1 Molecular statics calculations

All molecular statics calculations were performed using the LAMMPS code [51] with an interatomic potential adopted in this work developed by Li et al. [52] for the Nb-Mo-Ta-W system. The relaxed configurations were visualized using OVITO [53]. Initially, cells with a random distribution of Nb, Mo, Ta, and W in equal proportions were generated. The cells were oriented along $x = [111]$, $y = [1\bar{1}0]$, $z = [11\bar{2}]$ in a body-centered cubic (BCC) lattice with the dimensions of $49.6 \times 43.5 \times 41$ Å. Periodic boundary condition were enforced in all three dimensions. The total number of atoms inside the simulation cell ranged from 5600 to 5760.

1.2.2 Metropolis Monte-Carlo Method

To study the effect of short-range order (SRO) on vacancy energetics, we prepare simulation cells with a random distribution of atomic species and apply the Metropolis Monte-Carlo method to generate optimized atomic configurations at different temperatures. The Monte Carlo relaxations follow the sequence listed below:

1. Randomly choose a type of atom-pair with different atom species (e.g. Nb and Ta, Nb and Mo), and attempt swaps for 100 times for candidates that belong to the chosen type.
2. Run a conjugate gradient (CG) minimization of the structure at that point.
3. Repeat steps 1 and 2 until the total energy of the supercell converges with the number of iterations.

A series of temperatures ranging from 300 K to 1500 K are chosen and we then quantify the degree of SRO as determined by a pre-specified order parameter (discussed below).

1.2.3 Vacancy formation and migration energies

The vacancy formation energy, E_V^f , is calculated in the fashion of:

$$E_V^f = E_{N-1} - E_N + \mu_{avg} \quad (1.1)$$

where E_{N-1} and E_N are the total energies of relaxed supercells with and without a vacancy, respectively, and μ_{avg} is the chemical potential energy of the average alloy computed as:

$$\mu_{avg} = \frac{1}{4}(\mu_{Nb} + \mu_{Mo} + \mu_{Ta} + \mu_W) \quad (1.2)$$

where μ_i ($i = Nb, Mo, Ta, W$) is the chemical potential of a pure element calculated in the context of its pure metal.

Since E_V^f varies due to the change of local chemical environment in the alloy, up to 300 different lattice sites were randomly chosen for each cell to collect vacancy formation energies in as many local environments as possible. For the purpose of comparison, the vacancy formation energies in pure constituents of the alloy and the ‘average’ alloy (average across all four constituents) are also computed and analyzed.

For their part, vacancy migration energies, E_V^m , are calculated using the nudged elastic band (NEB) method implemented in LAMMPS. Vacancy trajectories along the first nearest neighbor direction [111] were subdivided into a total number of eight replicas, including six intermediate replicas plus the initial and final configurations. The NEB method furnishes the minimum energy path (MEP) from the initial to the final replica. After finding the MEP, the E_V^m is computed as the difference between the energy at the saddle point and the energy of one of the end replicas. Similar to the case of E_V^f , we try over 150 different lattice locations to capture the configurational variations introduced by the alloy compositional fluctuations.

1.3 Results

1.3.1 Equilibrium lattice parameter

To calculate the lattice parameter a_0 , we ran conjugate gradient minimizations of supercells containing 16000 atoms arranged into a random structure. Figure 1.1 shows the energy per atom as a function of the unit cell size, a . The error bars correspond to 20 independently generated random configurations for each value of a . A second-degree polynomial fit to the data yields a value of $a_0 = 3.243 \text{ \AA}$. Using the same method, we simulated the lattice parameters of the individual alloy constituents as well as their weighted average given in Table 1.1. As the results show, a_0 for Nb and Ta are 2.5% larger than the average value, while the values for Mo and W are 2.1% smaller.

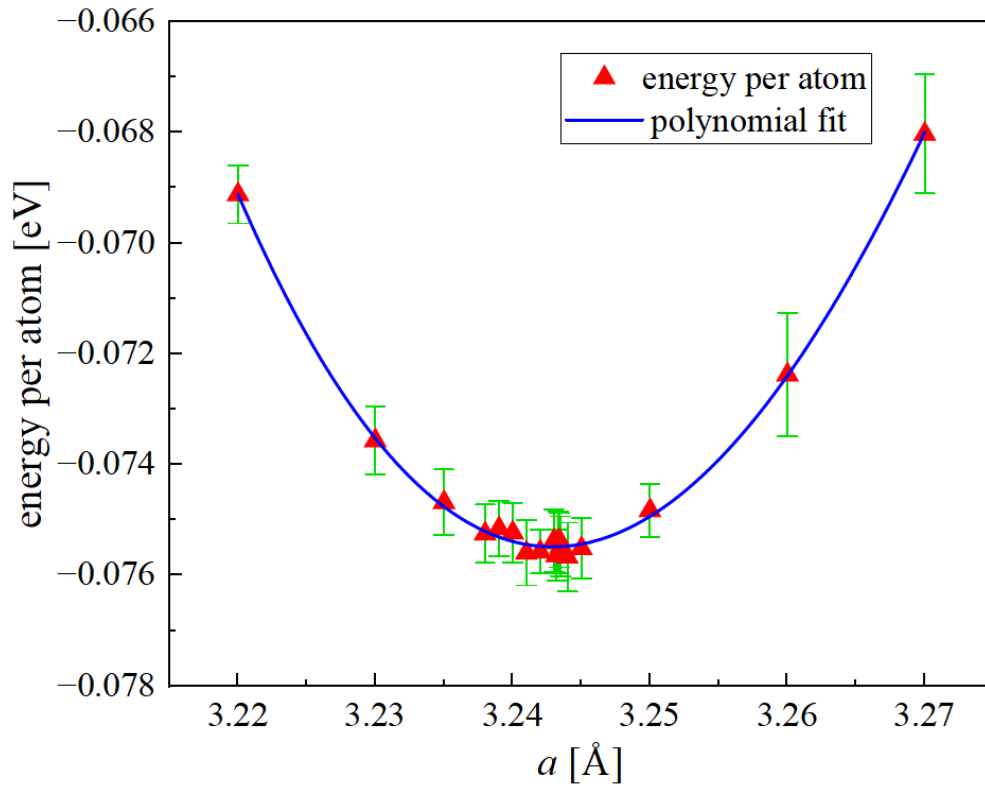


Figure 1.1: Potential energy per atom as a function of a for random equiatomic Nb-Mo-Ta-W.

Table 1.1: Simulated equilibrium lattice parameters of the random equiatomic Nb-Mo-Ta-W alloy, the 'average' alloy and the individual constituents metals.

Symbol	$a_0[\text{Å}]$
Nb-Mo-Ta-W	3.24
Nb	3.33
Ta	3.32
Mo	3.17
W	3.18
'average'	3.25

1.3.2 Short range order calculation

The degree of SRO is quantified by the Warren-Cowley parameter [54], defined as:

$$\eta_{\alpha\beta} = 1 - \frac{\sum_i^{N_\beta} x_i^{\alpha\beta}}{N_\beta c^\beta} \quad (1.3)$$

where $x_{\alpha\beta}$ is the local concentration of atoms of type α neighboring an atom of type β (here we consider only the first-nearest neighbor (1NN) shells), while c^β is the global concentration of atom species β in the cell. N_β is the number of atoms of type β in the computational cell. With this definition, there are 10 unique pairs, characterized by the following values:

$$\eta_{\alpha\beta} \begin{cases} < 0, & \text{ordering} \\ = 0, & \text{random} \\ > 0. & \text{separation} \end{cases} \quad (1.4)$$

The Warren-Cowley parameters of the system are computed as a function of temperature after Metropolis Monte Carlo relaxations of computational cells consisting of 5760 atoms. Figure 1.2 shows the evolution of the supercell energy as a function of temperature. Convergence is achieved within 150000 iterations at the highest temperatures, while it requires in

excess of 600000 steps below 900 K. The values for the 10 distinct pairs of elements are plotted in Figure 1.3 as a function of temperature. The small band around zero (‘error band’) marks the spontaneous SRO introduced by species fluctuations in the random configuration. In general, pairs of elements from the same group, either group VB or group VIB (e.g., Ta-Nb and Mo-W) tend to segregate from one another ($\eta_{\alpha\beta} > 0$), while pairs composed of elements from different groups (e.g., Ta-Mo, and Nb-W) show a tendency to ordering ($\eta_{\alpha\beta} < 0$). Among these, the pair Ta-Mo becomes the most negative one, indicating the strongest attraction between the two elements involved. Our calculations agree with results of previous SRO studies in the equimolar Mo-Nb-Ta-V-W system [55, 56]. Interestingly, at 300 K, the Warren Cowley parameter of Nb-Mo decreases slightly while that of Ta-Mo continues to increase, which suggests that a competition may exist between Ta and Nb when pairing with Mo.

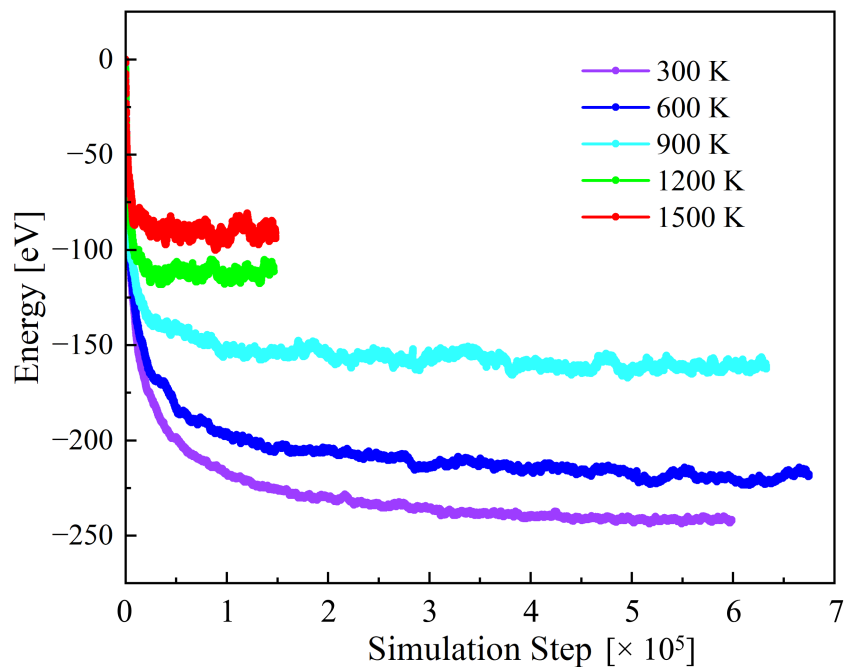


Figure 1.2: Energy evolution of the random Nb-Mo-Ta-W during annealing at different temperatures. The total energy of the system at the initial state is zero for easier reference.

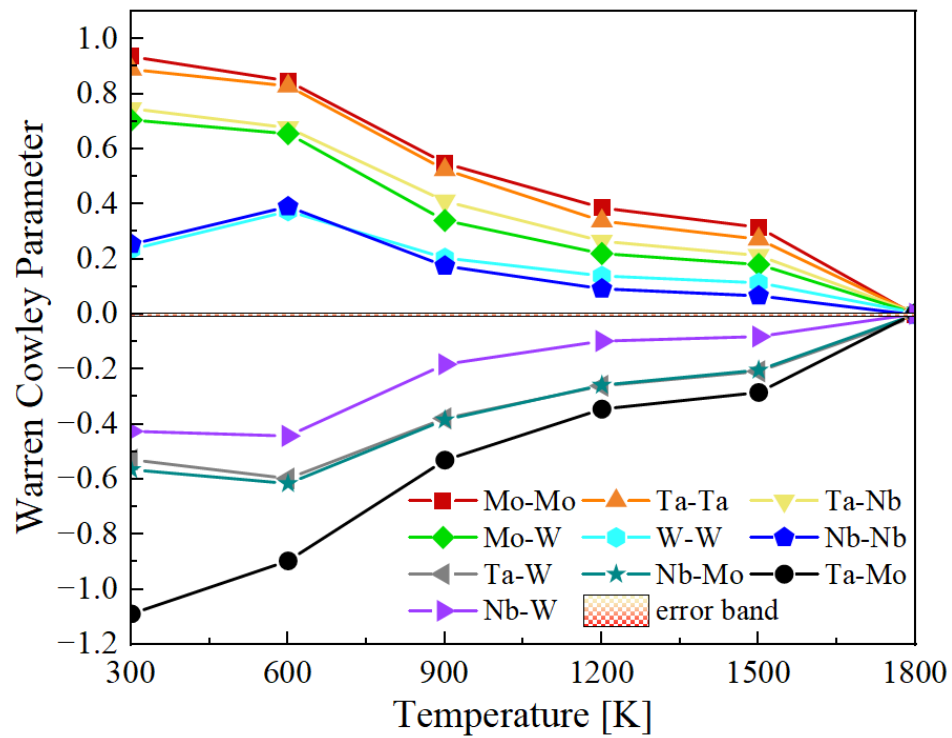


Figure 1.3: 1NN Warren Cowley parameter as a function of annealing temperature.

1.3.3 Vacancy energetics in bulk systems

1.3.3.1 Vacancy formation energies in bulk Nb-Mo-Ta-W

The chemical potential energies used in the calculation of vacancy formation energies in the real alloy is displayed in Table 1.2:

Table 1.2: The chemical potential energies of pure elements and the average alloy computed in the context of the pure metals. The 'average' represents the weighted average of chemical potential energies of Nb,Ta,Mo and W.

symbol	μ [meV]
Nb	6.1
Ta	13.4
Mo	22.3
W	21.3
'average'	15.8

To calculate the vacancy formation energy distributions, we collect data for up to 300 randomly distributed vacancies in each box with the corresponding SRO as obtained in the previous section. The E_V^f distributions of formation energies are shown in Figure 1.4. The dashed line in each figure represents the statistical mean of each distribution, which is listed in Table 1.3. Our results show that the effect of SRO on E_V^f is relatively weak, and that as the temperature increases, the random alloy becomes a good representative of the relaxed supercells with SRO. The vacancy formation energies of the constituent metals, as well as their arithmetic averages, are also presented in Table 1.3. Interestingly, the average of the individual constituent elements is noticeable larger than those of the actual alloy.

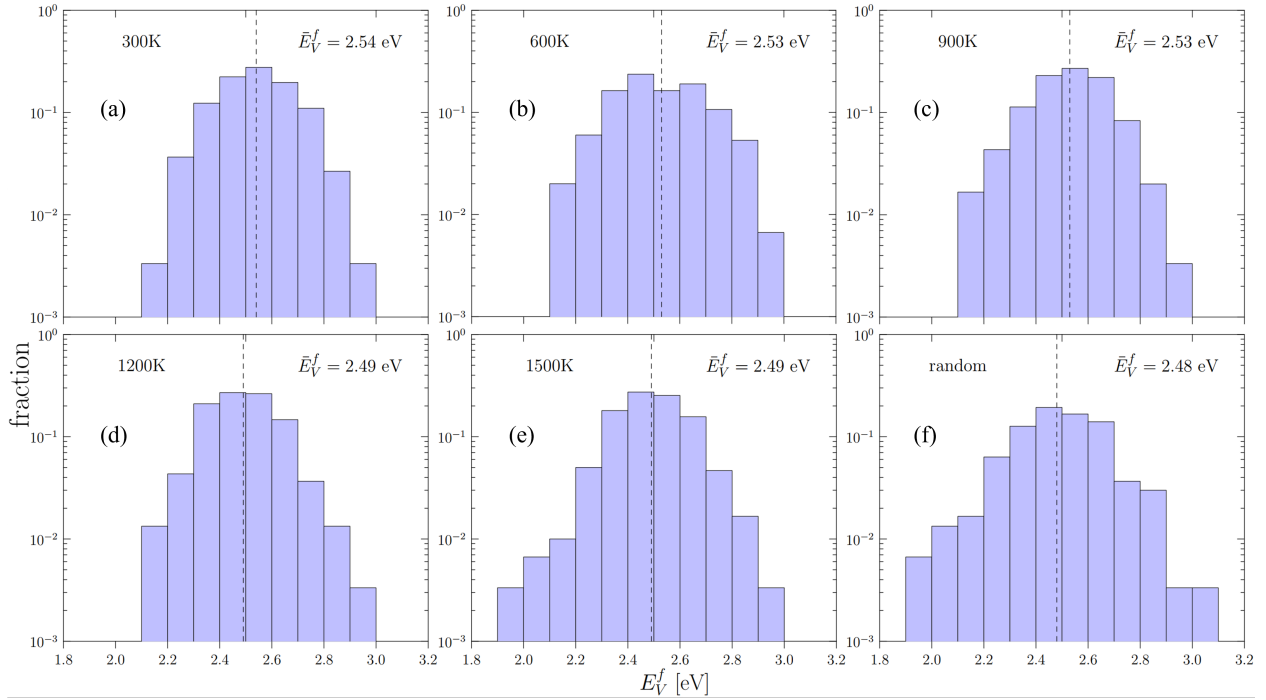


Figure 1.4: The distributions of vacancy formation energies of: **(a-e)** cells with SRO (annealing temperature from 300 K to 1500 K) and **(f)** the random cell of Nb-Mo-Ta-W. The dashed line shows the position of the statistical average of each distribution.

1.3.3.2 Effective vacancy formation energy in bulk

While the vacancy formation energy distributions given in Figure 1.4 represent the spectrum of possibilities for vacancies to form in a random lattice, in reality the thermal vacancy concentration is not well predicted by the distribution averages. This is because thermal sampling of the distributions disproportionately favors low energy occurrences. As such, it is of interest to calculate the equilibrium concentration of vacancies as a function of temperature, $C_V(T)$, by direct sampling of Figure 1.4.

Next, we visit a large number of lattice sites, $N=10^{10}$, and evaluate the Boltzmann probability of forming a vacancy by uniformly sampling the distributions given in Figure 1.4:

$$p_i = \exp\left(-\frac{E_i^f}{kT}\right) \quad (1.5)$$

Table 1.3: Statistical averages of vacancy formation energy distributions of Nb-Mo-Ta-W and vacancy formation energies of the pure constituents. The 'average' represents the weighted average of vacancy formation energies of Nb,Ta,Mo and W.

Alloy condition	E_V^f [eV]
300 K	2.54
600 K	2.53
900 K	2.53
1200 K	2.49
1500 K	2.49
random	2.48
Nb	2.32
Ta	2.24
Mo	2.81
W	2.93
'average'	2.57

where E_i^f is the i^{th} sampling of the vacancy formation energies, k is the Boltzmann constant. $C_V(T)$ is obtained as the ratio of the number of successful vacancy formation events, $n(T)$, defined by

$$\xi_i < p_i$$

where ξ_i is a uniform random number between 0 and 1., and the total number of trials, N , i.e.:

$$C_V(T) = \frac{n(T)}{N} \quad (1.6)$$

One then matches the calculated value of $C_V(T)$ to an 'effective' formation energy:

$$E_{eff}^f(T) = -kT \log \frac{n(T)}{N} \quad (1.7)$$

The effective formation energies at temperatures ranging from 1500 K to 2000 K are shown in Figure 1.5. The values are listed in Table 1.4. The value of E_{eff}^f starts from about 2.37 eV at 1500 K, and grows with a decreasing rate to approximately 2.40 eV at 2000 K. It is clear in the figure that the sensitivity of E_{eff}^f to temperature decreases beyond 1500 K which leads to slow increasing in E_{eff}^f , resulting in lower effective energies at all temperatures compared with the average E_V^f of the distribution in the random bulk. The significance of these calculations will be explained in the discussion session.

Table 1.4: The effective vacancy formation energies of Nb-Mo-Ta-W at different temperatures.

T [K]	E_{eff}^f [eV]
1500	2.367
1600	2.375
1700	2.383
1800	2.393
2000	2.398

1.3.3.3 Vacancy migration energies in the bulk

The minimum energy path (MEP) of vacancy migrations was obtained by the nudged-elastic band (NEB) method for all the pure elements and for the equiatomic Nb-Mo-Ta-W system. 150 different paths were analyzed for the alloy. The results are shown in Figure 1.6. As expected, the reaction path in the alloy is not symmetric, due to chemical energy differences between the initial and final states. As a result, two distinct barriers can be extracted from the alloy.

As in the previous section, the distributions of vacancy migration energy, E_V^m , of cells with and without SRO are shown in Figure 1.7. The mean values of E_V^m for all temperatures

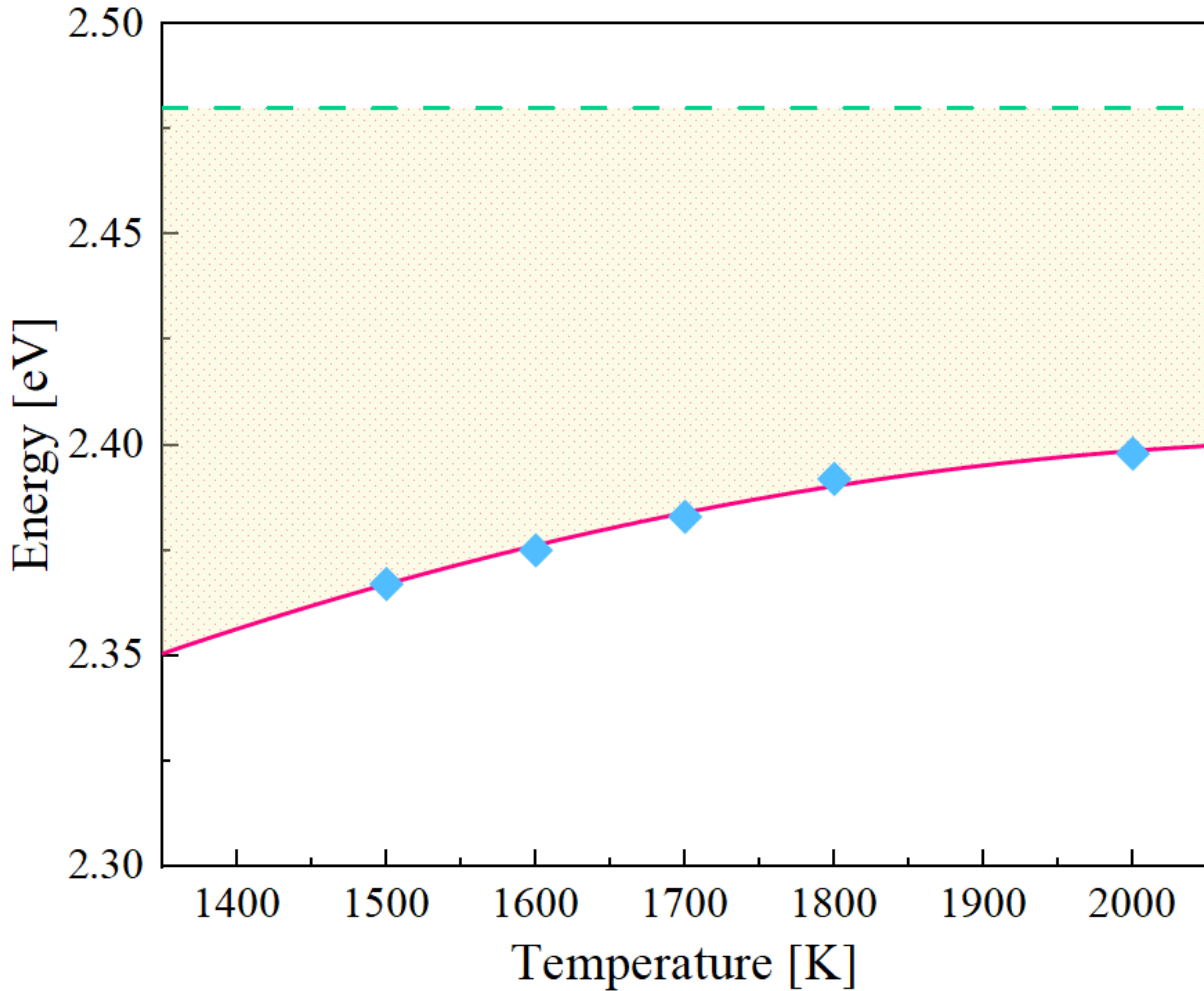


Figure 1.5: Effective vacancy formation energy as a function of temperature. The horizontal line represents the statistical average in the vacancy formation energy distribution of the random Nb-Mo-Ta-W bulk. The shadow region highlights the difference between effective energies and the statistical average value.

are given in Table 1.5. Here, a clear decrease in E_V^m can be seen with decreasing SRO.

To compare, the migration energies of pure components and the 'average' alloy are simulated and displayed in Table 1.5 as well. Among all the components, W has the highest migration energy as 2.074 eV which is higher than all Nb-Mo-Ta-W alloys, while other pure elements have close (e.g. Mo) or lower energies (e.g. Nb and Ta) than the Nb-Mo-Ta-W

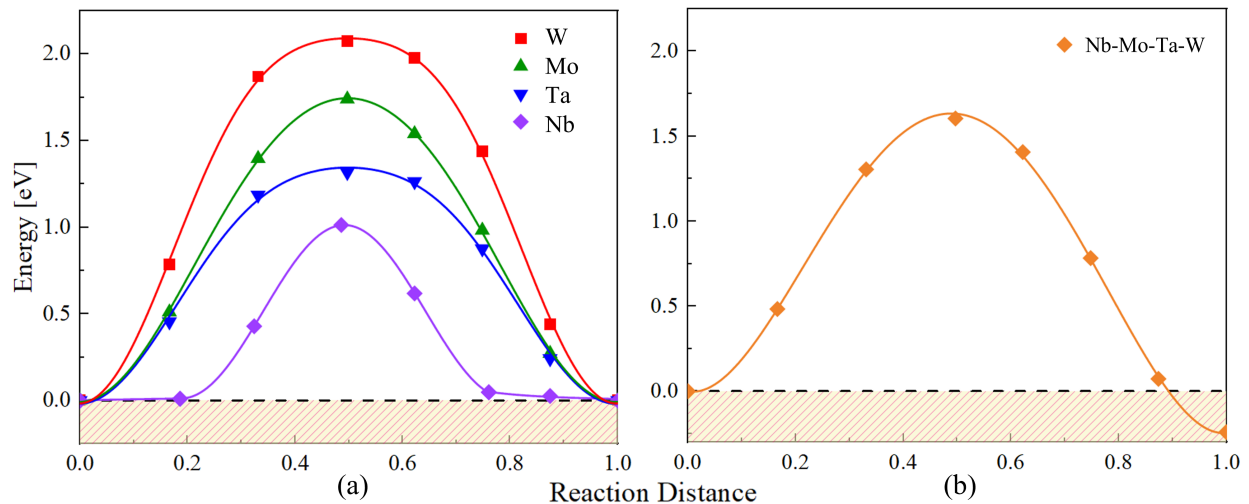


Figure 1.6: The MEPs of vacancy migration in (a) pure constituent metals and (b) the equiatomic random Nb-Mo-Ta-W.

alloys. The average of the four pure metals stands as 1.529 eV, smaller than the average migration energies of all the Nb-Mo-Ta-W alloys.

In the bcc crystal lattice, there are eight 1NN jumps originating from the same site. It is thus important to check if vacancy migration barriers are correlated to the originating site, or completely uncorrelated. To that end, we compute barriers purely randomly (i.e., select a lattice site at random and one 1NN path at random) or in a correlated fashion (one lattice site at random and all eight paths at that location). The results for both cases are shown in Figure 1.8. While slight differences exist, we see that there is no distinct difference between the energy distributions of the single direction and the eight-direction case. This suggests that the migration barriers are truly uncorrelated from the originating lattice site.

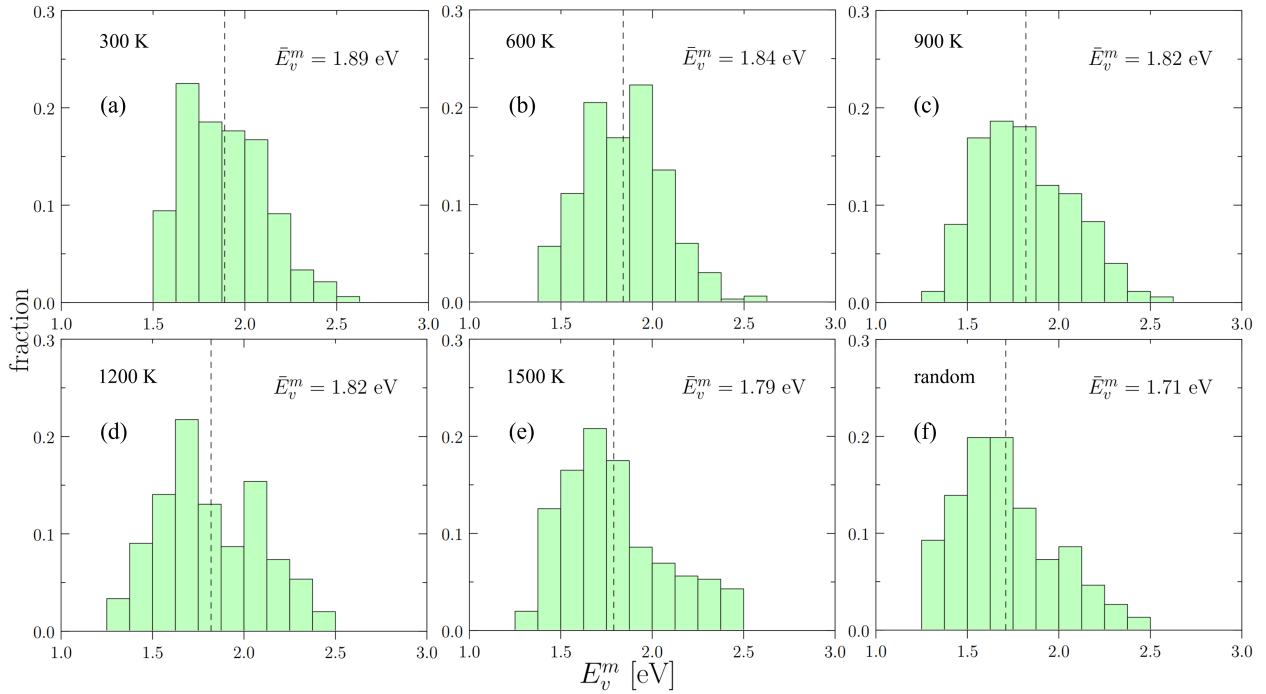


Figure 1.7: The distributions of vacancy migration energies of: (a-e) cells with SRO (annealing temperature from 300 K to 1500 K) and (f) the random cell of Nb-Mo-Ta-W. The dashed line shows the position of the statistical average of each distribution.

1.3.4 Vacancy energetics at edge dislocation cores

1.3.4.1 Formation energies

Vacancy formation is significantly facilitated by heterogeneities. A good example of structural heterogeneity is an edge dislocation. To this end, next we calculate the vacancy formation energies as a function of distance to an edge dislocation core on the atomic plane of the compressive region immediately adjacent to the glide plane. Figure 1.9 shows a relaxed $\frac{1}{2}[111]$ edge dislocation dipole with atoms colored by their chemical nature created as explained in the paper by Hossain et al. [57]. The figure also shows the locations where vacancy formation energies have been calculated. Figure 1.10 shows the results obtained from 300 independent evaluations. As shown, the vacancy formation energies are drastically reduced

Table 1.5: Statistical averages of vacancy migration energy distributions of Nb-Mo-Ta-W and vacancy migration energies of the pure constituents. The 'average' represents the weighted average of vacancy migration energies of Nb,Ta,Mo and W.

Alloy condition	E_V^m [eV]
300 K	1.89
600 K	1.84
900 K	1.82
1200 K	1.82
1500 K	1.79
random	1.71
Nb	0.99
Ta	1.32
Mo	1.74
W	2.07
'average'	1.53

within four Burgers vector distances from the bulk values around 2.5 eV down to 1.0 eV at position '0'.

As before, SRO only has a marginal effect on these results. The specific values at location '0' as a function of SRO at different temperatures and also for the elemental metals are given in Table 1.6. The formation energies for the Nb-Mo-Ta-W system are higher than those of the pure metals and the 'average' alloy.

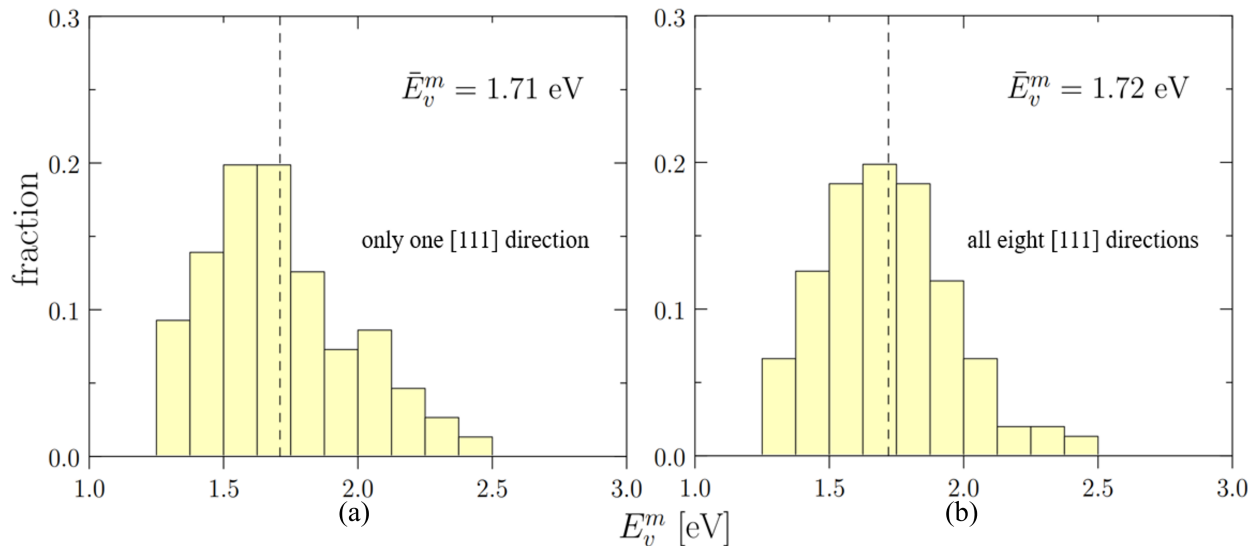


Figure 1.8: The distributions of vacancy migration energies when: (a) only one [111] direction is considered and (b) all eight directions of [111] type are considered.

1.4 Discussion

1.4.1 Statistical distribution of vacancy energetics

As displayed in Figure 1.4 and Figure 1.7, we find that both vacancy formation energies and migration energies are statistically distributed, which agree with observations in recent works in HEAs [29, 45, 58, 59]. The largely spread in the distributions can be explained by the variety of local chemical environments in the alloy. Our results also demonstrate that the spread width and average energies of both distributions of E_V^f and E_V^m display a minor but non-negligible dependence on SRO.

1.4.2 Analysis of vacancy formation energy and migration energy

Since the formation energy distributions are quite widely-spread, vacancies with large formation energies are rarely activated, resulting in the asymmetric thermal sampling towards low formation energies. Therefore, the effective formation energies should be lower than the

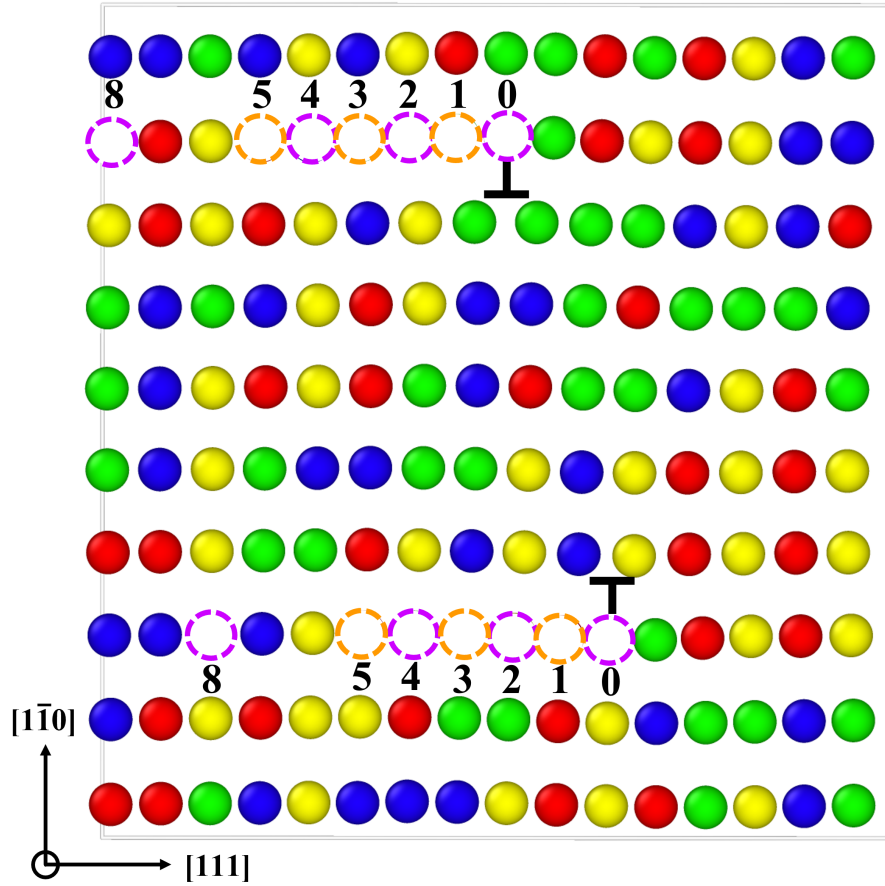


Figure 1.9: A cell of random Nb-Mo-Ta-W with an edge dislocation dipole. The ‘ \perp ’ symbols mark the exact locations of dislocation cores. The dashed circles indicate locations with varying atomic distances from dislocation cores (e.g. position ‘0’ is of zero interatomic distance from the core). Colors represent different atomic species: red = Ta, blue = Nb, yellow = Mo, green = W.

statistical averages of the formation energy distributions, which is confirmed by comparing the values of E_V^f (see Table 1.3) and E_{eff}^f (see Table 1.4). As temperature goes low, E_{eff}^f decreases with an increasing rate because the possibility of sampling vacancies with large barriers drops exponentially.

The presence of edge dislocation core effectively changes the formation energy barriers

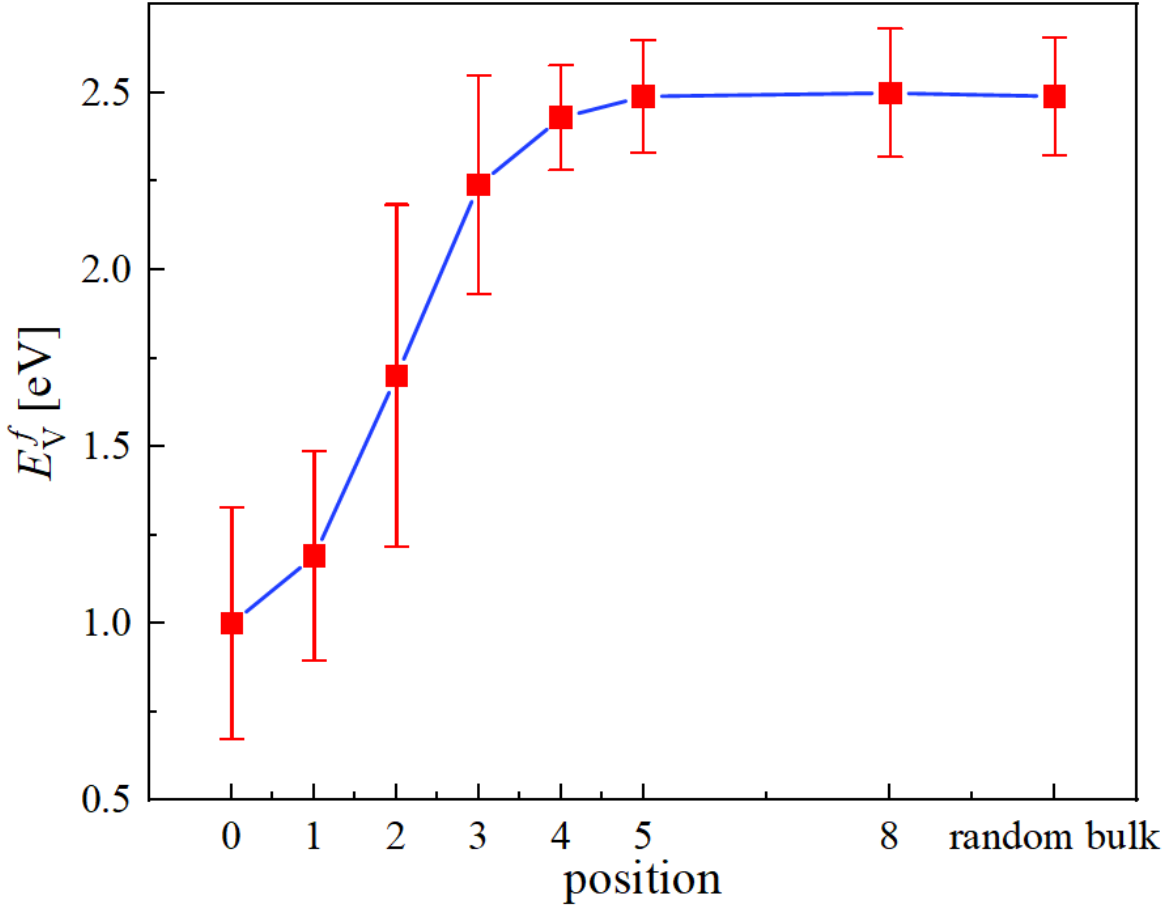


Figure 1.10: Vacancy formation energies as a function of distance from the edge dislocation core. The labeled positions in the x axis refer to the locations shown in Figure 1.9. The point labeled as 'random bulk' gives the formation energy obtained in Section 1.3.3.

of vacancies within a few Burgers vector distances from the core, and its effect becomes negligible once vacancies are beyond five Burgers vector distances from the dislocation core (see Figure 1.10). The formation barriers are reduced to below 1.0 eV on average at core in the compressive region (see Figure 1.9), with occasional occurrence of near-zero E_V^f .

Unlike E_V^f , the statistical averages of distributions of E_V^m adequately describe the barriers of migration. During migration, a vacancy can visit a variety of chemical environments over a long distance, which involves a great number of independent samplings of E_V^m with varying

Table 1.6: Statistical averages of vacancy formation energy distributions of position '0' in alloys with varying degrees of SRO. The 'average' represents the weighted average of vacancy formation energies at position '0' in Nb,Ta,Mo and W.

Alloy condition	E_0^f [eV]
300 K	1.11
600 K	1.12
900 K	1.05
1200 K	1.09
1500 K	1.10
random	1.00
Nb	0.86
Ta	0.81
Mo	0.94
W	0.97
'average'	0.90

values. Therefore, the value of stochastic average barrier of migration by sampling is close to the statistical average computed from the migration energy distribution.

1.4.3 Self-diffusion coefficients of Nb-Mo-Ta-W

Refractory high entropy-alloys are generally said to display *sluggish* diffusion [60, 61]. While this may be logically inferred from the known self-diffusion coefficients in the parent metals, here we have the opportunity to provide a direct assessment based on the results presented in this chapter.

We start with the general Arrhenius expression for the diffusivity of a substitutional

atomic species i :

$$D^i = D_0^i \exp\left(-\frac{\Delta H^i}{kT}\right) \quad (1.8)$$

where ΔH^i is the activation enthalpy and D_0^i is a temperature-independent diffusion pre-factor. ΔH^i is calculated as the sum of the formation and migration energies of a vacancy:

$$\Delta H^i = E_f^i + E_m^i \quad (1.9)$$

For Nb-Mo-Ta-W, we use the *effective* formation energies as the source for the values of E_f^i (from Fig. 1.5) since they describe the true thermal concentrations of vacancies in the alloy. In terms of E_m^i , the statistical averages do adequately represent the migration barrier (see Table 1.5). In particular, as we demonstrated in Sec. 1.3.3.3, the vacancy migration energies can be considered uncorrelated with the originating jump site, which simplifies the sampling of the distributions given in Fig. 1.8. The pre-exponential factors are computed using the expression:

$$D_0 = \frac{1}{6} z f \nu_0 b^2 \quad (1.10)$$

where $z = 8$ is the 1NN coordination number in bcc lattices, $f \approx 0.75$ is a correlation factor, $b = \frac{\sqrt{3}}{2} a_0$ is the 1NN jump distance and a_0 for different systems can be found in Table 1.1. ν_0 is the Debye frequency, which is computed as:

$$\nu_0^3 = 6\pi^2 n c^3 \quad (1.11)$$

where n is the atomic density, c is the velocity of sound in the material, expressed as:

$$n = \frac{2}{a_0^3} \quad (1.12)$$

$$c = \sqrt{\frac{K}{\rho}} \quad (1.13)$$

where K is the shear modulus, and ρ is the mass density, computed using the equation:

$$\rho = \frac{2m}{N_A a_0^3} \quad (1.14)$$

where m is the atomic weight, 2 represents the number of atoms per unit cell in bcc structure, $N_A = 6.022 \times 10^{23}$ is the Avogadro’s constant. Values of D_0 and parameters used for computing the diffusivity of each system are listed in Table 1.7. At the moment, we do not have parameters in eq.(1.10) specific for the alloy, and thus we simply use a simple average of the values of the pure constituent metals. As such, the relevance of D_0 for this study is very marginal and is only used for estimation purposes.

Table 1.7: Parameters and pre-exponential factors used in calculation of diffusivity.

System	K [GPa] [52]	m [a.m.u.] [62]	D_0 [$\times 10^{-6}$ m ² ·s ⁻¹]
Nb-Mo-Ta-W	83	138.41	2.96
Nb	32	92.91	2.39
Ta	59	180.95	2.31
Mo	110	95.95	3.86
W	160	183.84	3.40

Figure 1.11 shows an Arrhenius plot of the diffusivities of the elemental metals and the Nb-Mo-Ta-W system for both the effective vacancy concentrations and the distribution averages. The figure clearly shows that the diffusivities of the pure metal and the alloy (in the two alternatives considered) are extremely low, thus substantiating the notion of sluggish diffusion typically attributed to RHEA.

1.4.4 Comparison with other works

In a recent MD study by Luke [50], the average formation energy of a vacancy in random Nb-Mo-Ta-W was given as 2.26 eV, which is consistent with our result of 2.48 eV. Similar values are also obtained in ternary equiatomic V-Ta-W [63], which display an average value of 2.81 eV. In another work by Byggmatar et al. [56], an average formation energy of 3.3 eV was obtained in Mo-Nb-Ta-V-W using density-functional theory (DFT) calculations,

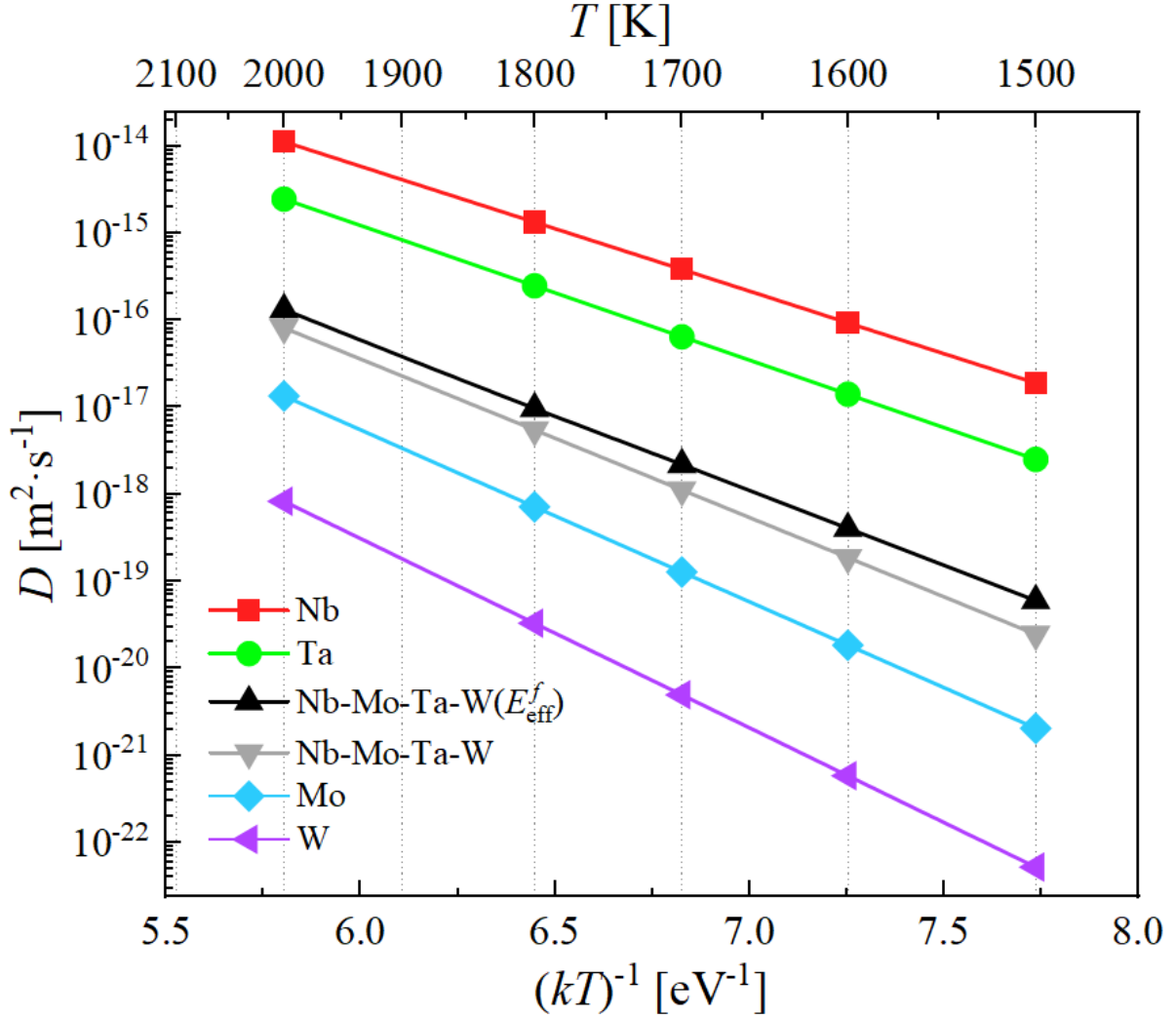


Figure 1.11: Diffusivities of Nb-Mo-Ta-W and its pure constituents as a function of temperature.

and 3.1 eV using the Gaussian approximation potential framework. Using DFT, Roy et al. [64] studied vacancy stability in the body-centered cubic $(Mo_{0.95}W_{0.05})_{0.85}Ta_{0.10}(TiZr)_{0.05}$ and computed the average formation energies ranging from 3.4 eV to 3.52 eV by alternating chemical environment. All their observations agree with our findings about the effect of SRO on vacancy energetics, i.e., the variation of E_V^f and E_V^m as a function of the local environment.

As for vacancy migration, a recent work of the ternary equiatomic bcc Mo-Nb-Ta alloy

by Xing et al. [48] shows that when SRO is introduced into the system the chemical ordering induces a localizing trapping effect which increases the migration energies. This is in agreement with our results (Fig. 1.7). They also report a broadening with SRO of the migration energy distributions, which in contrast is not so clear-cut in our case.

A study by Wang et al. [65] shows that the equilibrium concentrations of vacancies are greatly enhanced by the high entropy in the HEAs compared to pure metals, which corresponds to our finding that the effective formation energy of Nb-Mo-Ta-W is smaller than the average value of E_V^f obtained from its pure constituents especially at temperatures lower than 1600 K.

1.5 Conclusions

We end the chapter with our most important conclusions.

1. Both vacancy formation and migration energies in Nb-Ta-Mo-W are defined by statistical distributions with a wide spread, on the order of 1.0 eV in some cases.
2. Vacancy energetics in Nb-Mo-Ta-W display a non-negligible dependence on SRO, which is reflected by the decrease in E_V^f from 2.54 eV to 2.48 eV and E_V^m from 1.89 eV to 1.71 eV as SRO weakens with increasing temperature.
3. The vacancy formation energies are reduced by 1.4 eV on average as they approach an edge dislocation core from the bulk. Vacancies with low energies near zero can be found at core positions, from which we hypothesize the formation of ‘superjogs’ on edge dislocation lines would be easy.
4. Due to the wide spread distribution of vacancy formation energies, its thermal sampling becomes asymmetric towards lower values, resulting in lowering in effective vacancy formation energies compared to statistical averages in formation energy distributions.

5. The effective diffusivity in Nb-Mo-Ta-W using E_{eff}^f is smaller than the diffusivities of Nb and Ta, however larger than those of Nb-Mo-Ta-W using the statistical average E_V^f as well as Mo and W, the value of which starts from $10^{-19} \text{ m}^2 \cdot \text{s}^{-1}$ at 1500 K to $10^{-16} \text{ m}^2 \cdot \text{s}^{-1}$ at 2000 K, confirming the sluggish diffusion reported in the equimolar Nb-Ta-Mo-W alloy.

CHAPTER 2

Self-interstitial Configurations, Energetics and Diffusive Properties in the Equiatomic Nb-Mo-Ta-W Alloy

2.1 Introduction

Refractory multi-element alloys (RMEA) are a special class of materials composed of typically four or more refractory metal elements, such as Nb, Mo, Ta, V, W, Cr, Hf, or Zr, mixed in near equal proportions. These alloys generally crystallize into a simple body-centered cubic (BCC) phase and are found to retain high strengths up to high temperatures [16, 22–27, 66], making them attractive candidates as structural materials in the power, aerospace, or nuclear sectors [11–13, 67, 68]. Among these, the equiatomic Nb-Mo-Ta-W system has become a model alloy of the RMEA group due to its phase stability, microstructural simplicity, and mixture of elements with high lattice distortion, making it an ideal experimental and computational test bed to study fundamental behavior [7, 9, 16, 21, 66, 69].

The refractory nature of these alloys endows them with a high melting temperature, high defect formation energies, and high threshold displacement energies [49, 56, 65, 70, 71]. Consequently, RMEA are being actively considered as irradiation-tolerant materials in nuclear environments [11, 72–76]. However, at the macroscopic level, irradiation resistance is linked primarily to time-dependent phenomena such as swelling, hardening, and embrittlement [77]. Key to the connection between atomic-scale properties and macroscopic behavior is the role

of point defects, i.e., self-interstitial atoms (SIA) and vacancies. Generally, when SIA clusters become decoupled from vacancy clusters, a recombination imbalance occurs and the excess defect concentration can lead, over time, to microstructural evolution and material property changes [77–82]. This decoupling can take place by a number of different mechanisms, such as vacancy cluster dissolution and/or immobilization, or large vacancy-SIA cluster mobility disparity. Indeed, in pure metals and dilute alloys, SIA clusters are known to undergo fast quasi one-dimensional (1D) diffusion along rectilinear trajectories punctuated by sporadic orientation changes [83–92]. As SIA clusters grow larger, which is typically favored by higher irradiation energies and by the thermodynamics of defect aggregation, these orientation changes become rarer, leading to purely one-dimensional motion and full vacancy-SIA decoupling. Thus, two of the general approaches for enhancing radiation resistance are (i) to diminish the propensity of SIA clusters of a given size to migrate in 1D or (ii) to inhibit the formation of large SIA clusters for a given irradiation energy. Recent studies indicate that in concentrated multi-element alloys, large SIA cluster formation is indeed inhibited relative to pure metals [63, 76, 93]. Likewise, SIA cluster migration is seen to be significantly more constrained. Potentially, all this points to an intrinsic radiation resistance in RMEA not seen in their pure element or dilute alloy counterparts. Here, we explore the properties of SIA defects in the Mo-Nb-Ta-W system, for which no results have been published yet.

The starting point of our study is the structure of single self-interstitials. In crystalline solids, SIA generally adopt ‘split’ configurations oriented along dense atomic crystal directions. In BCC metals, these are $\langle 111 \rangle$ or $\langle 110 \rangle$ orientations [80, 91, 94–100]. Thus, it is of interest to study whether the intrinsic chemical disorder and lattice distortion typical of RMEA changes this general picture and what the implications for radiation resistance may be. Recent work has focused on Mo-Nb-Ta-W-V [56, 71], V-Ta-Cr-W [49], and Ti-V-Ta-Nb [101] systems, as well as in the ternaries V-Ta-Ti and V-Ta-W [63, 93], all using recently-developed data-driven machine-learning interatomic potentials [52, 102, 103]. The main focus in these studies was to calculate the formation energies of the corresponding split

α - β SIA configurations (where α and β denote chemical elements), which are seen to display large variabilities both with respect to one another and as a function of the local chemical environment for a given α - β pair. Note that, in complex concentrated alloys, the very notion of ‘self’-interstitial atom is misleading, as all atoms are potentially different from each other, even in the split configuration. However, for convenience, we will continue to refer to them as “SIA” or “self-interstitials”.

In this work we calculate single self-interstitial formation energies for five distinct topological configurations and all elemental pairs in Nb-Mo-Ta-W alloys. We also calculate their diffusivity and study the trajectories of each SIA defect under thermal diffusion conditions to ascertain the dimensionality of their motion and their migration properties. The chapter is organized as follows. First, we discuss the atomistic simulation method, including the details of construction of the random Nb-Mo-Ta-W model and the methods for calculating SIA formation energies, E_{SIA}^f . We then present results for E_{SIA}^f for all SIA types considered, and calculations of the mean square displacement and the diffusion coefficient. This is followed by a discussion of the results to calibrate the impact of our findings and their implications in terms of the radiation tolerance of Nb-Mo-Ta-W. We finish the chapter with our most important conclusions.

2.2 Methods

2.2.1 Atomistic calculations

All the atomistic calculations were performed using the LAMMPS code [51] with the interatomic potential developed by Li et al. [52] for the Nb-Mo-Ta-W system. The relaxed configurations were visualized using OVITO [104]. Initially, cells with a random distribution of Nb, Mo, Ta, and W in equal proportions were generated. The cells were oriented along $x = [111]$, $y = [1\bar{1}0]$, $z = [11\bar{2}]$ in a BCC lattice with the dimensions of $49.6 \times 43.5 \times 41$ Å. Periodic boundary condition were enforced in all three dimensions. The total number of atoms inside

the simulation cell ranged from 5600 to 5760.

2.2.2 Defect energy calculations

One of the unique aspects of complex concentrated alloys (CCA) is that point defect energies are characterized by statistical distributions instead of single-valued functions. For self-interstitials, this is evident in the expression used to calculate the SIA formation energy:

$$E_{SIA}^{\alpha-\beta} = E_T^{\alpha-\beta} - (E_0 + \mu_\alpha) \quad (2.1)$$

where $E_{SIA}^{\alpha-\beta}$ is the formation energy of a SIA formed by an extra atom of type α an existing lattice atom of chemical type β ($\alpha, \beta = \text{'Nb'}$, 'Mo' , 'Ta' , or 'W'), $E_T^{\alpha-\beta}$ is the total energy of the computational cell containing $N + 1$ atoms, E_0 is the total energy of a cell of N atoms, and μ_α is the chemical potential of an atom of chemical type α in the alloy. As the expression indicates, variations in the energy of a supercell composed of N atoms can occur due to different atomic configurations for the same nominal alloy composition. This can be accounted for by considering a statistically-significant number of different configurations of the Nb-Mo-Ta-W alloy, and averaging over the entire space of configurations tried. In addition, the SIA formation energy depends specifically on the chemical nature of both the extra atom added to the lattice and the host atom occupying it. This requires knowing in advance the four chemical potentials of the alloy, which can be calculated by ‘flipping’ the chemical nature of one atom for that of another, and then calculating the change in energy, $\Delta E^{\alpha \rightarrow \beta}$, for the total computational cell [105]. Mathematically:

$$\Delta\mu^{\alpha \rightarrow \beta} = \mu_\beta - \mu_\alpha = \Delta E^{\alpha \rightarrow \beta} - E_0 \quad (2.2)$$

The system is fully defined by the energy and mass balance conditions:

$$E_0 = N_{Nb}\mu_{Nb} + N_{Mo}\mu_{Mo} + N_{Ta}\mu_{Ta} + N_W\mu_W \quad (2.3)$$

$$N = N_{Nb} + N_{Mo} + N_{Ta} + N_W \quad (2.4)$$

Equations (2.2), (2.3), and (2.4) conform a system of equations that can be solved running molecular statics calculations in random alloy supercells. Table 2.1 gives the calculated chemical potentials for the Nb-Mo-Ta-W alloy obtained from 130 independent configurations of a computational cell of 24192 atoms containing a random equiatomic alloy. Also shown are the values calculated for each pure element (using the same interatomic potential). Equipped with this information, one can now calculate the formation energies of the pertinent SIA combinations.

Table 2.1: Calculated chemical potentials for the equiatomic Nb-Mo-Ta-W alloy and the pure elements. The results for the alloy were extracted from 130 independent alloy configurations in supercells containing 24192 atoms. The last two columns give the lattice parameters of the pure elements and the lattice distortion relative to pure W: $\delta = (a_0^\alpha - a_0^W) / a_0^W$.

α	μ_α (pure metal) [eV]	$\bar{\Delta}\mu^{\alpha\rightarrow\beta}$	$\bar{\mu}_\alpha$ (in Nb-Mo-Ta-W alloy) [eV]	a_0 [Å]	δ [%]
Nb	-7.8123	-0.0124	-7.8222	3.3265	4.6
Mo	-6.8786	-0.0856	-7.0248	3.1667	-0.5
Ta	-8.0434	-0.1477	-8.1289	3.3183	4.3
W	-7.9495	-0.0563	-7.9966	3.1812	0.0

As indicated above, in metals, SIA ordinarily adopt linear configurations along high-density atomic chains. However, in complex concentrated alloys with large lattice distortion, other possibilities for accommodation of extra atoms may emerge around regions with increased local atomic volume. Consequently, in this work we consider five main configurations: tetrahedral, octahedral, and split dumbbells along the $\langle 110 \rangle$, $\langle 110 \rangle$, and $\langle 100 \rangle$ directions. Figure 2.1 shows a schematic representation of these structures as a reference.

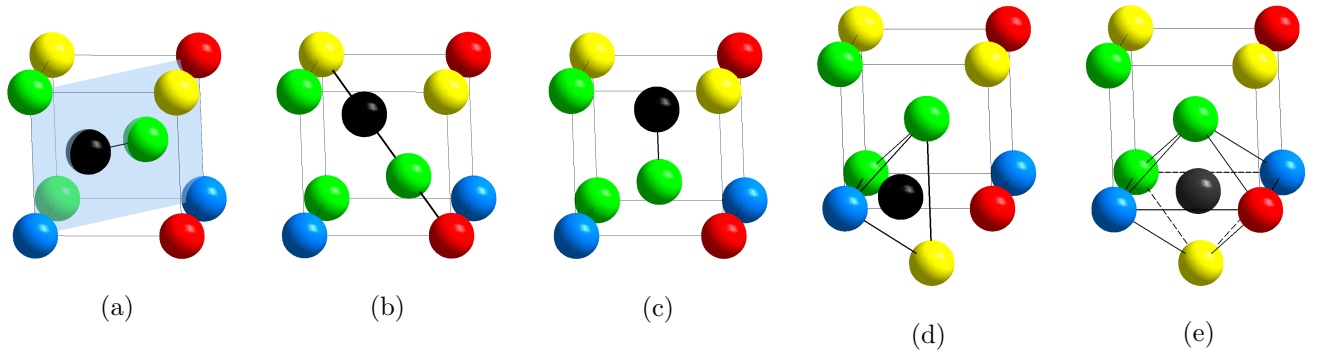


Figure 2.1: Split dumbbell configurations in BCC crystals: (a) $\langle 110 \rangle$ orientation, (b) $\langle 111 \rangle$ orientation, and (c) $\langle 001 \rangle$ orientation. (d) and (e), tetrahedral and octahedral configurations. The atom colored in black represents the extra atom that forms the self-interstitial configuration.

2.3 Results

2.3.1 Formation energies of self-interstitial atoms

2.3.1.1 SIA defects in the pure metals

Before embarking on a detailed study of SIA structures in the Nb-Mo-Ta-W system, it is helpful to get a reference for the atomistic model employed in this work by calculating the SIA formation energies in each one of the four elemental metals separately. Table 2.2 gives the formation energies of the $\langle 111 \rangle$ SIA configurations in each of the pure metals. The table includes calculations from other sources for comparison with the SNAP potential and cross-verification.

As the table shows, the energies obtained with the SNAP potential for the pure elements are in reasonable agreement with other independent calculations. It is worth noting that the SNAP potential did not include SIA formation energies as part of the parameter database that it was fitted with.

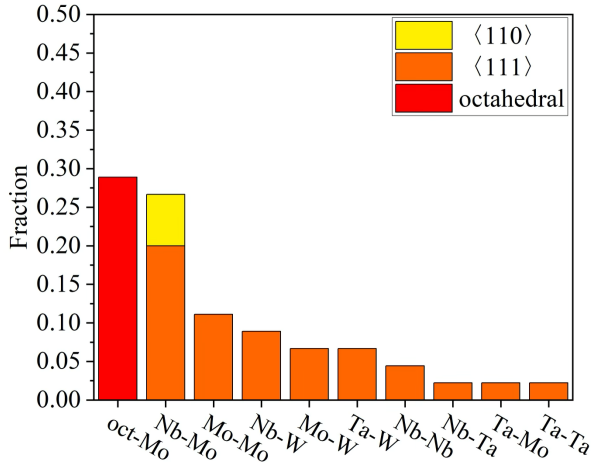
Table 2.2: SIA formation energies for the $\langle 111 \rangle$ configurations in the elemental metals calculated in this work using the SNAP potential (in bold text), and published in other works. ‘DFT’: density functional theory. ‘BOP’: bond-order potentials. All energies are in eV.

Element	This work (SNAP)	DFT calculations [99]	BOP [106]	Other studies
Nb	4.38	4.79	5.25	
Mo	6.49	7.42	5.83	7.34 [107]
Ta	6.31	5.84	7.42	6.37 [108]
W	9.77	9.55	9.50	9.82 [109]

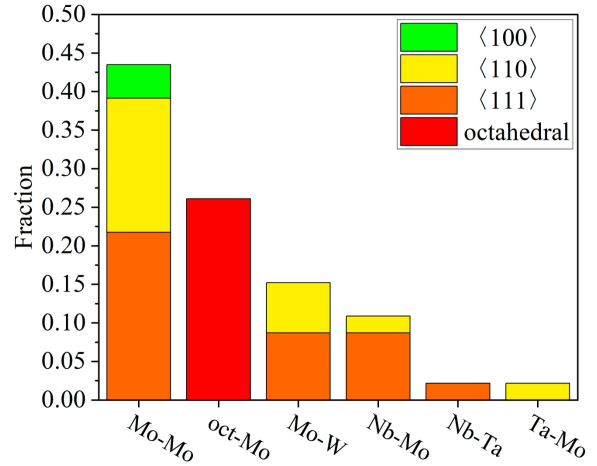
2.3.1.2 SIA defects in Nb-Mo-Ta-W

Next, we insert one extra atom at a random location in the atomistic supercell and let the system relax using a simulated annealing. We then look at the structure of the resulting self-interstitial and tally up the results. We repeat this process 400 times, 100 per each atomic species. Figure 2.2 shows the normalized histograms corresponding to each of the 100 cases of same species, while Figure 2.3 gives the combined histogram for all 400 cases combined. Visual inspection of these figures leads to the following main observations:

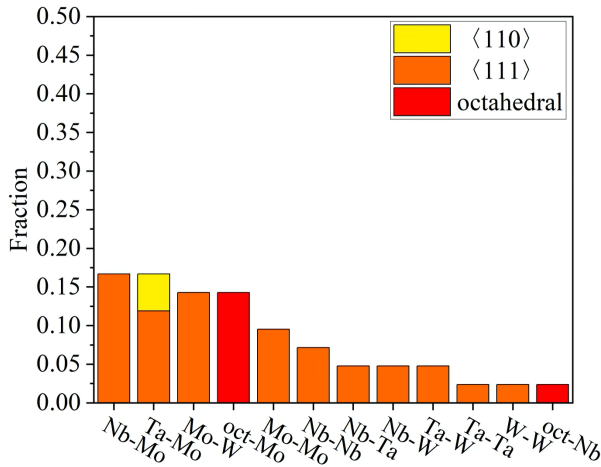
1. There is a clear preference for Mo-containing self-interstitials, with Mo-Mo, octahedral Mo, Mo-Nb, and Mo-W being the most stable, in that order, among all SIA structures observed. Mo-Mo, Mo-Nb, and Mo-W are all found adopting $\langle 111 \rangle$ configurations as their most common state.
2. Of the octahedral self-interstitials, oct-Mo is most frequent.
3. Of the three split SIA configurations, $\langle 111 \rangle$ are always more common, followed by $\langle 110 \rangle$, and then by $\langle 100 \rangle$. This is a general observation, irrespective of the specific atom pair forming the SIA.



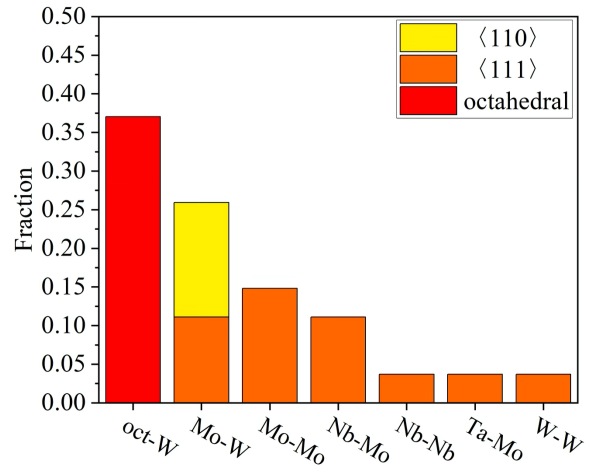
(a) Nb



(b) Mo



(c) Ta



(d) W

Figure 2.2: Normalized histograms of the final configurations observed in random Nb-Mo-Ta-W alloys for insertions of the same type of atomic species (indicated under each subfigure). Note that insertion of an extra atom of species α does not necessarily have to lead to a self-interstitial containing that same species.

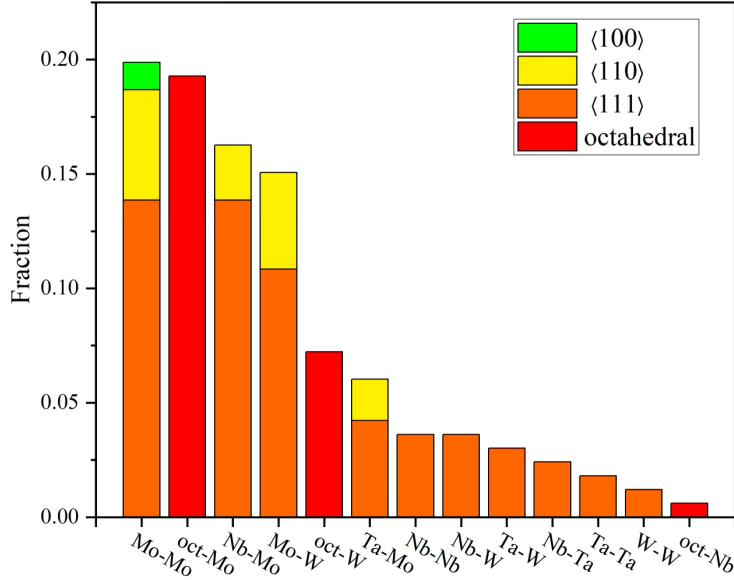


Figure 2.3: Relative occurrence of each type of SIA structure observed after relaxation.

- Self-interstitials not containing a Mo atom are a factor of two rarer than those with Mo.

To confirm that occurrence correlates with energetic stability, next we calculate the formation energies of all the observed SIA structures. Figure 2.4 shows a violin plot organized by both the chemical species involved in the SIA and their crystallographic orientation. In general, Figs. 2.3 and 2.4 are consistent with one another, i.e., SIA energy correlates directly with occurrence. The only exception is the octahedral Mo self-interstitial, which, with values between 7.0 and 8.0 eV, have significantly higher formation energies than much rarer SIA such as Ta-Mo or Nb-Nb.

To first order, we can correlate the atomic size (in terms of the lattice distortion it creates, see Table 2.1) with the relative occurrence of each SIA structure. First, our results are generally consistent with Mo being the smallest and least energetically costly atom, as

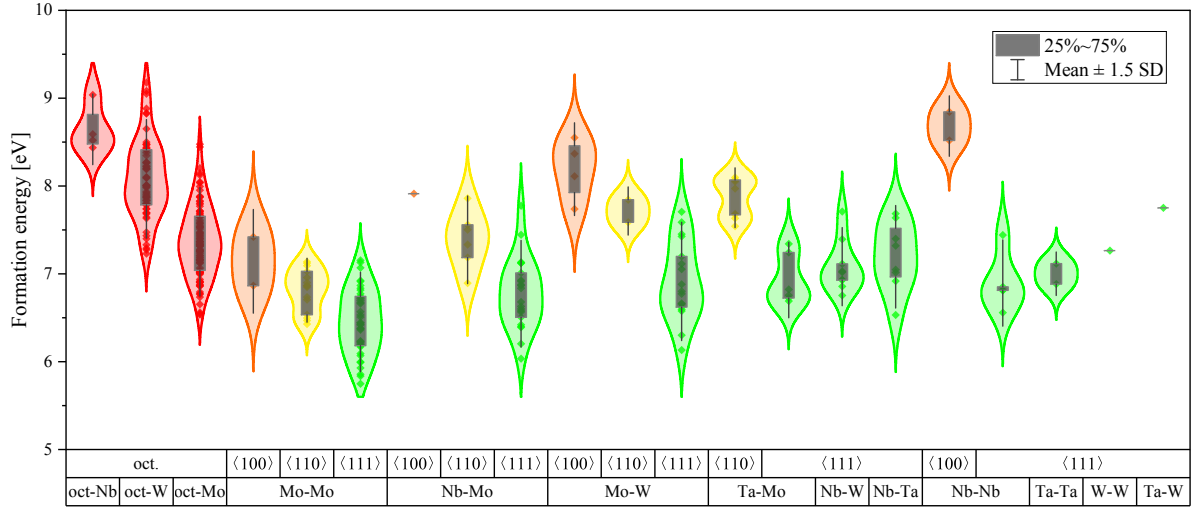


Figure 2.4: Violin plot showing the SIA formation energies in random Nb-Mo-Ta-W alloys for all structures observed. Octahedral configurations are placed on the left (no ‘oct-Ta’ structures were stable), followed by the energies of the $\langle 100 \rangle$, $\langle 110 \rangle$, and $\langle 111 \rangle$ configurations for split SIA pairs. ‘SD’ stands for “standard deviation” (in the legend).

evidenced by the high occurrence of octahedral-Mo and Mo-Mo SIAs. Mo also couples well to the oversized atoms Nb and Ta, mostly in the $\langle 111 \rangle$ configuration, which would suggest that the Mo-Ta and Mo-Nb SIA accommodate well in the crystal by canceling their respective lattice distortions. This coupling between atoms with a small and a high lattice distortion does not seem to apply to the Ta-W SIA. As well, combining the two smallest atoms, Mo and W, into a SIA also does seem to be favored, as seen in the relatively low formation energies of the $\langle 111 \rangle$ Mo-W SIA.

2.3.2 Diffusion of self-interstitial atoms in Nb-Mo-Ta-W

Diffusion of self-interstitials is studied in the usual manner, i.e., by allowing the defect to carry out a spontaneous random walk at a given temperature and then calculating the mean

square displacement, $\langle \Delta R^2 \rangle$, as a function of time:

$$\langle \Delta R^2 \rangle = \frac{1}{M} \sum_i^M [\mathbf{r}_i(t) - \mathbf{r}_i(0)]^2 \quad (2.5)$$

where $\mathbf{r}_i(0)$ is the initial position of the defect, and $\mathbf{r}_i(t)$ is its position at time t , which must be tracked over a statistically significant time period (one nanosecond in our case). M represents the number of independent simulations at each temperature (five in our case). The SIA diffusivity is then obtained from the slope of the $\langle \Delta R^2 \rangle$ -vs- t curves as a function of time [86, 110]:

$$D_{SIA}(t) = \frac{1}{2n} \frac{d}{dt} [\langle \Delta R^2 \rangle(t)] \quad (2.6)$$

where n is the dimensionality of the SIA migration ($n = 1, 2, \text{ or } 3$). This equation is predicated on the equivalency of diffusive jumps in a uniform medium, i.e., on the onset of a truly random walk. However, in complex chemical environments, the SIA defect will not generally see crystallographically-symmetric diffusion paths and thus it is not clear that the linear $\langle \Delta R^2 \rangle$ -vs- t assumption holds. Instead, here we monitor the instantaneous value of $D_{SIA}(t)$ until it converges in time. Prior to that, however, we must determine the defect diffusion dimensionality, n , by tracking the position of the defect as a function of time and constructing its spatial trajectory. Exemplars of such trajectories at 900, 1500, and 2000 K are shown in Figure 2.5. We observe a clear shift in diffusion dimensionality from one-dimensional ($n = 1$) at 900 K and below to three-dimensional ($n = 3$) at 1200 K and above. This shift is qualitatively consistent with the behavior of SIA in pure metals, where SIA diffusion paths are too seen to occur along $\langle 111 \rangle$ directions, with sporadic changes of orientation that increase in frequency with temperature.

With the value of n pre-established, next we plot the evolution of D_{SIA} with time as a function of temperature in Figure 2.6. As the figure shows, while 1 ns is generally not sufficient to lead to time-converged diffusivities (except at 2000 K), all the $D_{SIA}(t)$ curves monotonically decrease towards their corresponding asymptotic (i.e., time converged) values. Consequently, we fit all curves to the expression $D_{SIA}(t) = a(1 + bt^{-1})$, where a (asymptotic

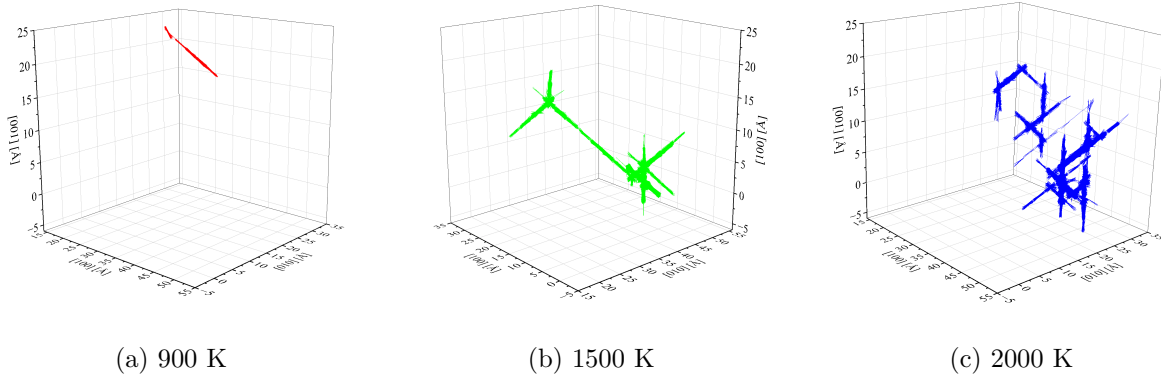


Figure 2.5: Spatial trajectories of SIA defects at different temperatures in equiatomic Nb-Mo-Ta-W alloys.

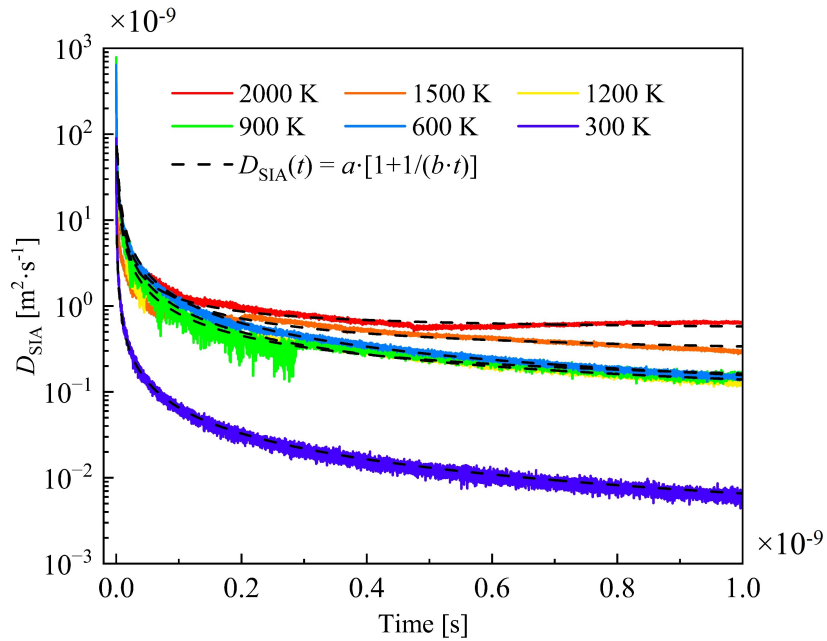


Figure 2.6: Evolution with time of the diffusivity of self-interstitial atoms at several temperatures. Dashed lines indicate asymptotic fits at each temperature.

value) and b (inverse time constant) are fitting parameters. Here, a represents the time-independent value of the diffusivity, while the constant b accounts for the initial transient

until steady state conditions have been established. The different values of a as function of temperature are then added to an Arrhenius plot, with the results shown in Figure 2.7.

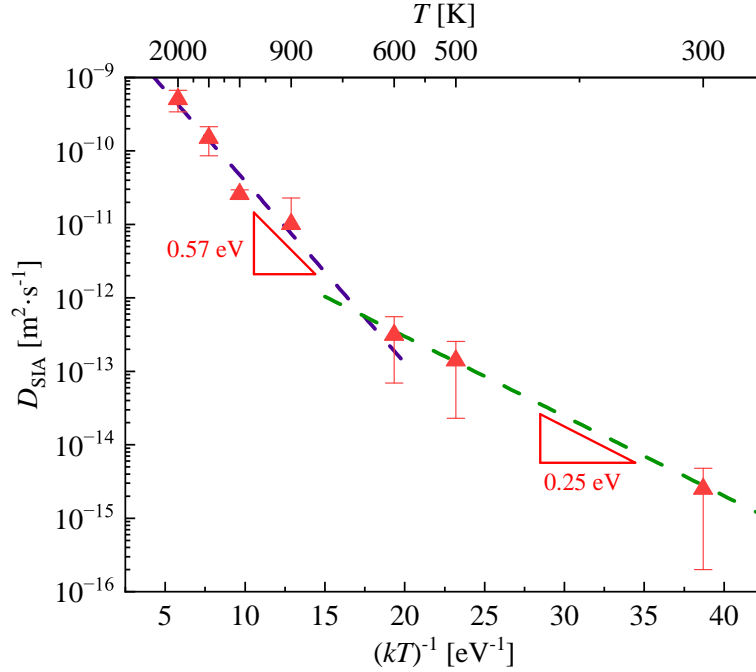


Figure 2.7: SIA diffusivities as a function of inverse temperature. Orange and blue dashed lines are fits to eq. (2.7) separating the 1D and 3D diffusing temperature regions.

Clearly, the data points are arranged into two clearly differentiated temperature regions. These regions are consistent with the split in diffusion dimensionality observed in Fig. 2.5, namely, 1D and 3D diffusion at low and high temperatures, respectively. Accordingly, we fit the values in each region separately to the classical expression:

$$D_{SIA}(T) = D_0 \exp\left(-\frac{E_m^{SIA}}{kT}\right) \quad (2.7)$$

where D_0 is the diffusion pre-factor, and E_m^{SIA} is the migration energy. The values of D_0 and E_m^{SIA} obtained from the fits in each region are given in Table 2.3. The differences in these values can also be explained by the defect migration mode. At low temperatures (≤ 600 K), diffusion is primarily one-dimensional and, as such, the value of E_m^{SIA} (0.25 eV) reflects

Table 2.3: Diffusion parameters extracted from Fig. 2.7.

parameter	$T \leq 600 \text{ K}$	$T \geq 600 \text{ K}$
$D_0 \text{ [m}^2\cdot\text{s}^{-1}\text{]}$	4.43×10^{-11}	1.16×10^{-8}
$E_m^{SIA} \text{ [eV]}$	0.25	0.57

the transition barrier for migration along the $\langle 111 \rangle$ direction. Such process is generally understood to be mediated by a soft vibrational mode and thus represented by a relatively low energy barrier. Indeed, this is the dominant migration mechanism observed in pure metals, which correspondingly display low values of E_m^{SIA} as shown in Table 2.4 for Mo, Nb, Ta, and W. However, the value of D_0 in this regime is several orders of magnitude smaller than those of the pure metals given in the table ($\sim 10^{-11}$ vs. $10^{-8} \text{ m}^2\cdot\text{s}^{-1}$).

Above 600 K, the SIA experiences more frequent rotations between different $\langle 111 \rangle$ directions, turning defect migration into a three-dimensional process. Rotation is also a thermally activated process defined by its own transition energy, often higher than that of the pure translational process [85, 111, 112]. To first order, one can estimate the rotational energy barrier as the difference between the total, 0.57 eV, and the translational barrier, 0.25 eV, which gives $\Delta E_{rot}^{SIA} \approx 0.32 \text{ eV}$. The diffusivity pre-factor in this case is on the order of those found in pure metals ($\sim 10^{-8} \text{ m}^2\cdot\text{s}^{-1}$).

Table 2.4: Pre-exponential factors and SIA migration energies found in the literature for the pure elements Nb, Mo, Ta, and W.

parameter	Nb	Mo	Ta	W
$D_0 \text{ [m}^2\cdot\text{s}^{-1}\text{]}$	9.4×10^{-8}	3.8×10^{-7}	1.0×10^{-8}	2.2×10^{-7}
$E_m^{SIA} \text{ [eV]}$	0.12	0.40	0.10	0.36, 0.02
source	[113]	[113]	[114]	[110], [115–117]

The literature on SIA diffusion in other RMEA is scarce [101, 118–120], limiting the opportunities for comparison. Zhao et al. [101] found migration energies for self-interstitials in the 0.18~0.28-eV range and pre-factors on the order of $\sim 10^{-8} \text{ m}^2 \text{ s}^{-1}$ in ternary (Ti-V-Ta) and quaternary (Ti-V-Ta-Nb) BCC alloys. Shi et al. [119] studied SIA motion in BCC Nb-Zr-Ti at 1200 K and found a diffusivity of $3.88 \times 10^{-11} \text{ m}^2 \cdot \text{s}^{-1}$, approximately 15 times slower than in pure Nb. These studies are qualitatively consistent with ours in terms of showing reduced diffusivities in increasingly complex concentrated alloys relative to pure elements or dilute systems.

2.4 Discussion

The behavior of point defects is central to the theory of radiation damage [121–124]. Point defects are subjected to different biases in how they are produced and how they migrate, which over time leads to microstructural evolution in irradiated materials. As such, understanding their fundamental energetics (formation and migration) is the starting point for mounting a more comprehensive irradiation damage analysis. With recent advances in complex concentrated alloy development, the study of irradiation effects in chemically inhomogeneous systems is being pursued with renewed vigor. As well, given the inherent natural superiority of BCC metals over FCC ones in terms of irradiation tolerance, novel BCC refractory concentrated alloys are inviting new interest for nuclear applications [11, 73, 74]. In this work, we have calculated the energetics of self-interstitial atoms in Nb-Mo-Ta-W, which—as of the writing of this chapter—has not been the subject of a dedicated study.

One of the most important findings of this work is the high occurrence of octahedral self-interstitials in Nb-Mo-Ta-W. This is at striking odds with calculations in pure BCC metals [99, 125–127] and dilute BCC alloys [87, 91, 128–130], where the octahedral structure is the highest energy of all SIA configurations or outright unstable. Interestingly, however, octahedral self-interstitials are the most stable SIA configurations in hexagonal close-packed

(HCP) metals [131–133]. However, unlike in HCP metals, octahedral SIA in Nb-Mo-Ta-W are likely to be trapped in their geometric configurations, ultimately contributing to a low overall mobility. Finally, no SIA structure was found to be stable in a tetrahedral configuration, all converting to either $\langle 111 \rangle$ or $\langle 110 \rangle$ orientations.

Several studies have found that SIA and SIA cluster mobilities in complex concentrated alloys to be significantly lower than those of pure metals and dilute alloys [134, 135]. This too is the case in Nb-Mo-Ta-W, where SIA defects are seen to display diffusivities between 10^{-14} and $10^{-10} \text{ m}^2\cdot\text{s}^{-1}$ in the 300-to-2000 K temperature interval (Fig. 2.7). Below 600 K, SIA migrate one-dimensionally along $\langle 111 \rangle$ directions with an activation energy of 0.25 eV. This is in opposition to the practically athermal (i.e., virtually zero migration barrier) crowdion mechanism commonly found in pure metals, and seems to be owed to a transport mechanism characterized by transitions across multiple trapping sites (perhaps even including octahedral configurations). As the temperature increases above 600 K, SIA in Nb-Mo-Ta-W show an inclination to undergo changes in orientation, resulting in an activation energy of 0.57 eV. This higher energy likely includes the rotational energy barrier, which –to first order– can be obtained as the difference between the activation energies in both temperature regions. While such transformation from 1D to 3D-dominant migration is also common in pure metals [101], it is often not so clearly revealed in Arrhenius plots as it is here, with two clearly distinguishable regimes characterized by different pre-factors and activation energies. It is reasonable to assume that such marked differences are directly related to the introduction of chemical complexity into the alloy, as several studies in concentrated binary systems have demonstrated [91, 92, 101].

In all, when taken in conjunction with practically zero vacancy mobility in the entire temperature spectrum [136], we believe that SIA diffusivities may be too low, particularly below 900 K, to quantitatively contribute to mass transport during irradiation in Nb-Mo-Ta-W. This can lead to two diverging situations:

1. At or below 600 K, all damage produced in displacement cascades remains ‘frozen-in’

inside crystal grains. This limits opportunities for microstructural evolution, such as swelling, creep, etc., but is likely to lead to high hardening levels. This in turn will result in potentially severe loss of fracture toughness (which is generally low at low homologous temperatures in these materials to begin with). Optionally, the damage energy will have to be relieved by a phase transformation or amorphization.

2. The second scenario involves delayed recombination and self-healing, aided by the increased three-dimensionality of self-interstitial mobility in Nb-Mo-Ta-W above 600 K. With sufficient time, this will favor recombination with vacancies and reduced damage accumulation.

This could conceivably paint a scenario where the Nb-Mo-Ta-W alloy displays a sharp transition at 600 K from poor to excellent irradiation tolerance. It is interesting to note that the temperature at which SIA atoms are mobilized is commonly taken as the starting point of stage II in resistivity recovery experiments using isochronal annealing [137], which is generally in the vicinity of 120 K in pure refractory metals such as W [138]. Thus, a temperature of 600 K would signify a significant departure in RMEA from those in standard recovery stages during isochronal annealing in metals. Indeed, the limited experimental evidence we have in irradiated refractory (BCC) RMEA reveals a complex picture, with self-healing processes occurring in conjunction with amorphization and/or grain refinement [139–141]. From a thermodynamic point of view, this suggests that, at some critical dose, the high relative energy associated with the creation of Frenkel pairs is more efficiently relieved by other means of microstructural transformation. In any case, studies such as the present one underscore the importance of continuing to investigate all aspects of irradiation damage in complex alloys.

2.5 Conclusions

We finish with a summary of the main points of the chapter:

1. We have studied the entire spectrum of SIA formation energies and the SIA diffusion coefficient in Nb-Mo-Ta-W alloys. For this purpose, we have used a machine-learned interatomic potential specifically designed for Nb-Mo-Ta-W.
2. The formation energies of SIA are seen to vary significantly depending on the atom(s) involved in the defect. By far, Mo-containing SIA are the most frequently-occurring defects. The least likely atomic species to be found forming part of a SIA are Ta and W atoms.
3. The lowest energy geometric configuration corresponds to $\langle 111 \rangle$ split orientations. Octahedral Mo SIA are among the most stable structures, in contrast with BCC metals (more in accordance with what is found in HCP metals).
4. We have found two clearly distinguishable temperature regimes where the SIA diffusion changes dimensionality from 1D to 3D. We have calculated the migration energies and diffusion pre-factors in both regions, from which we have extracted the translational and rotational components of the defect migration. We find values of 0.25 eV and pre-factors of $\sim 10^{-11} \text{ m}^2 \cdot \text{s}^{-1}$ at temperatures below 600 K, and 0.57 eV and $\sim 10^{-8} \text{ m}^2 \cdot \text{s}^{-1}$ between 600 and 2000 K, and estimate the rotational energy barrier at 0.37 eV.

CHAPTER 3

Kinetic Monte Carlo (kMC) Modeling of Screw Dislocation Motions in the Equimolar Nb-Mo-Ta-W Alloys

3.1 Introduction

Refractory multi-element alloys (RMEA) are a special class of materials that generally crystallize into a simple body-centered cubic (bcc) phase and are found to display exceptional strengths to very high temperatures [16, 22–27, 66]. Among these, the equiatomic Nb-Mo-Ta-W system has become a model alloy of the RMEA group due to its phase stability and microstructural simplicity, making it an ideal experimental and computational test bed to study mechanical behavior [7, 9, 16, 21, 66, 69]. While the deformation mechanisms of bcc metals and their alloys are relatively well understood, theories that explain the behavior observed in body-centered cubic RMEA have only recently begun to be developed [142–146]. While these theories are helpful in establishing the strength of the alloy to first order, questions remain regarding aspects of dislocation motion in these materials. Of particular interest is the role played by screw dislocations, due to their preponderant role in the general theory of bcc plasticity, and how this role is modified in compositionally-complex settings [145, 147–150]. For example, it is believed that chemical fluctuations reduce the importance of kink-pair nucleation, shifting it instead to kink lateral motion. As well, it is yet not clear what are the slip mechanisms leading to such high strengths at high temperature in certain RMEA [1, 16, 52, 66, 69, 151, 152].

To investigate the above points and to complement existing statistical theories, we simulate the motion of screw dislocations in equiatomic and Nb-Ta-V and Nb-Mo-Ta-W alloys using a kinetic Monte Carlo model that has been previously applied to pure, dilute, and concentrated bcc systems [153–156]. The chapter is organized as follows. First, we provide the theoretical framework for the kinetic Monte Carlo model. This is followed by a description of the numerical implementation and modifications of the kMC simulator to adapt it to the alloy of choice. We then calculate dislocation velocities and present results of the strength of the alloy as a function of temperature. We finalize this chapter with a discussion of the results and the conclusions.

3.2 Methodology

We use a kinetic Monte Carlo (kMC) model specifically developed to study the time dynamics of long screw dislocation lines with Burgers vector \mathbf{b} in bcc systems. Dislocations are composed of connected discrete segments of finite length on a lattice oriented along the [111] direction. The dislocation moves by (i) nucleating kink-pairs on any of the {110} planes belonging to the [111] zone, or (ii) lateral kink motion along the [111] direction on those planes. Kinks are identified by their non-screw character, and are tracked in space and time during every iteration of the simulation. Stress fields are calculated using a non-singular isotropic elastic formulation [157]. While kink segments are represented as straight edge segments for visualization, for the calculation of internal stresses they are considered to extend over a distance a along the [111] direction and thus deviate from the pure screw orientation just by an angle of $\theta = \arctan(h/a) \approx 10^\circ$, where h is the wavelength of the Peierls potential.

Simulations can be done with periodic boundary conditions or with finite-sized lines. Unless otherwise noted, here we use dislocation lines of length $L = 500b$ pinned at both ends to mimic the operation of a Frank-Read source in the material. Shear stress is applied such that the (1 $\bar{1}$ 0) plane is always the maximum resolved shear stress (MRSS) plane. The

method has been applied to pure W [158], W substitutional (5% at. Re) and interstitial (0.1% at. O) alloys [154, 155]. Next, we present the aspects of the underlying theory that are specific to Nb-Mo-Ta-W alloys. As explained in ref. [156], the model employed to describe a multicomponent alloy involves the superposition of an effective substrate (often referred to as the ‘average’ alloy) whose properties are taken as the compositional average of each of the individual element properties, and a set of lattice atoms representative of the chemical composition of the alloy. As such, the kink-pair nucleation enthalpy is written as a sum that includes ‘solute’ interaction energies:

$$\Delta H_{kp}(\tau) = (\Delta H_0 + \Delta E_{x \rightarrow x+h}^{int}) \left(1 - \left(\frac{\tau}{\tau_P} \right)^p \right)^q \quad (3.1)$$

where ΔH_0 is the formation energy of a pair of isolated complementary kinks in the average alloy, $\Delta E_{x \rightarrow x+h}^{int}$ is the change of ‘chemical’ energy across one Peierls valley (i.e. between x and $x+h$) on a given dislocation segment i (with length ℓ_i), τ_P is the Peierls stress of the average alloy, and p and q are fitting parameters. The total nucleation rate on that segment is then given by:

$$J_{kp}^i(\tau; T) = \nu_0 \left| \frac{\ell_i - w}{b} \right| \exp \left(-\frac{\Delta H_{kp}(\tau)}{kT} \right), \quad \ell_i > w \quad (3.2)$$

where w is the kink separation in a kink pair, ν_0 is an attempt frequency, k is Boltzmann’s constant, and T is the absolute temperature. Similarly, kink motion is itself a thermally activated process with activation energy equal to $\Delta E_{y \rightarrow y+b}^{int}$, i.e. the excess energy that results when kinks move an amount b along the y (i.e., [111]) direction:

$$\omega_k(T) = \nu_1 \exp \left(-\frac{E_m + \Delta E_{y \rightarrow y+b}^{int}}{kT} \right) \quad (3.3)$$

where ν_1 is an attempt frequency not necessarily equal to ν_0 , and E_m is the migration energy for kink translation. $\omega_k(T)$ represents the hopping rate of a kink segment going from a position y to another $y+b$ separated by a barrier ΔE_k and ‘corrected’ by a term $\Delta E_{y \rightarrow y+b}^{int}$ that reflects the local chemical environment. In eqs. (3.1)-(3.3), the dependence on stress is through the resolved shear stress (RSS), τ , which is a scalar quantity that represents the

local projection of the total stress tensor $\boldsymbol{\sigma}$ on the glide plane of the dislocation, including non-Schmid effects if appropriate. $\boldsymbol{\sigma}$ contains contributions from the externally applied stress and from the different dislocation segment stress fields, as described in refs. [157, 158]. Equations (3.2) and (3.3) are then sampled according to the kMC algorithm for any available dislocation segment with length greater than w and for all existing kinks. Defined in this way, ΔH_{kp} and ω_k capture both elastic and inelastic effects, which allows for a rigorous treatment of both dislocation segments and point defect-like entities such as kinks, cross-kinks, vacancies, and self-interstitial atoms. The full list of variables for this purpose is given in Table 3.1, along with their source.

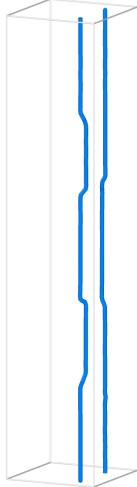
In eqs. (3.1) and (3.3), $\Delta E_{x \rightarrow x+h}^{int}$ and $\Delta E_{y \rightarrow y+b}^{int}$ represent the excess energies associated with the change in chemical environment during the motion of dislocation segments. As such, they are calculated for a specific spatial arrangement of lattice atoms, which must reflect the chemical complexity of the alloy. Examples of these environments are given in Figures 3.1a and 3.1b for the calculation of $\Delta E_{x \rightarrow x+h}^{int}$ and $\Delta E_{y \rightarrow y+b}^{int}$, respectively.

3.3 Results

3.3.1 Stress-free dislocation line relaxations

We first study the ground state of long dislocation lines as a function of temperature. The starting dislocation configuration is a straight line with a total length of $500b$. We then relax the lines by enabling thermally activated processes in the kMC model in the absence of applied stress. Convergence is understood in a steady-state sense, i.e., when the concentration of kinks is seen to just oscillate around a constant mean value [156]. The relaxed configuration of the dislocations is highly tortuous at all temperatures, containing high concentrations of kinks and cross-kinks on multiple glide planes. An example is given in Figure 3.2a, which shows a section of the line at 900 K displaying a very complex structure. This is consistent with the observation of ‘rough’ lines modeled in atomistic simulations of RMEA

Table 3.1: Parameters needed for eqs. (3.1)-(3.3). The values for ΔH_0 and τ_P are obtained as weighted averages of the pure element values as calculated in ref. [2]. The image in the rightmost column shows the relaxed structure of a screw dislocation dipole in the random solid solution (only the dislocation lines are depicted). The length of the lines is equal to $80b$. Several kink pairs can be seen to emerge in the ground state of the dislocation lines.

Symbol	Value	Units	Source	Configuration
a_0	3.24	Å	[136]	
b	$\sqrt{3}/2$	a_0	-	
μ	83.0	GPa	[52]	
ν_0	0.09	THz	[156]	
ΔH_0	1.26	eV	[2]	
τ_P	1.41	GPa	[2]	
a	5	b	this work	
E_m	0.43	eV	[146]	
w	5	b	this work	
p	0.5	-	[159]	
q	1.25	-	[159]	

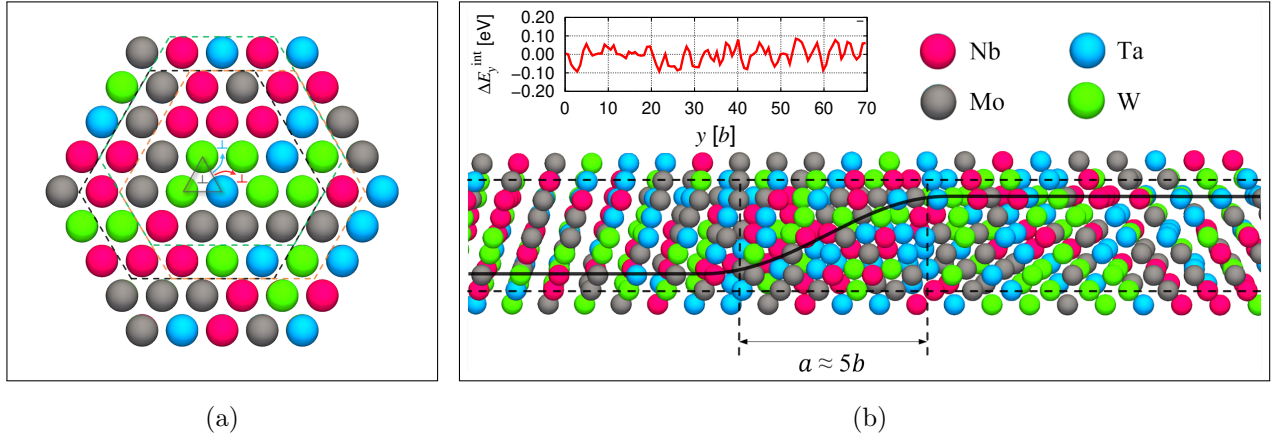


Figure 3.1: (a) View of the dislocation core along the [111] direction showing the minimal atomic environment needed to capture all kink-pair nucleation events. The dashed polygons represent the maximum extent of dislocation-atom interactions. (b) Spread of a single kink along the [111] direction indicating the region over which the interaction energy is calculated. For clarity, only atoms immediately surrounding the two adjacent Peierls valleys are shown. The inset to the figure shows the variation of $\Delta E_{y \rightarrow y+b}^{int}$ along a path of length $70b$ to showcase the rough chemical energy landscape encountered by kinks during their motion.

[142, 160–162]. However, extracting the precise nature and location of the features that contribute to this roughness in atomistic configurations is significantly more difficult.

We repeat this process 10 times with independent random seeds and count the number of total kinks, n_k , and cross-kinks. Note that the number of cross-kinks is a subset of the total number of kinks. We then plot the statistical average and error bars of all the counts at each temperature and plot the results in Arrhenius form in Figure 3.3.

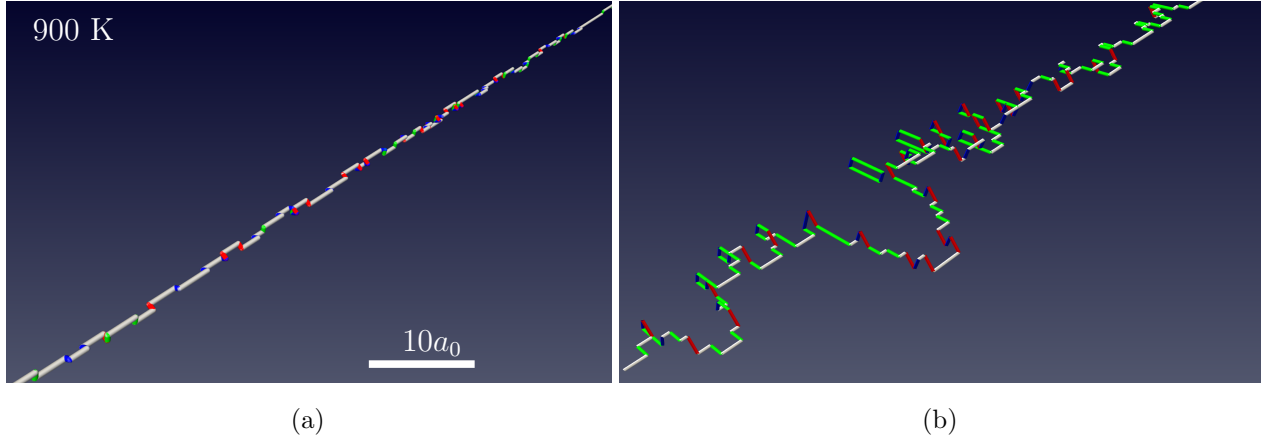


Figure 3.2: (a) Dislocation configuration after thermalization at 900 K. Kinks and cross-kinks emerge spontaneously during equilibration on all available $\{110\}$ planes. (b) Line configuration after 1 μ s of dislocation motion under 800 MPa of applied stress. Screw segments are colored in gray. All other segments are color-coded according to their glide plane. The size marker is common to both images

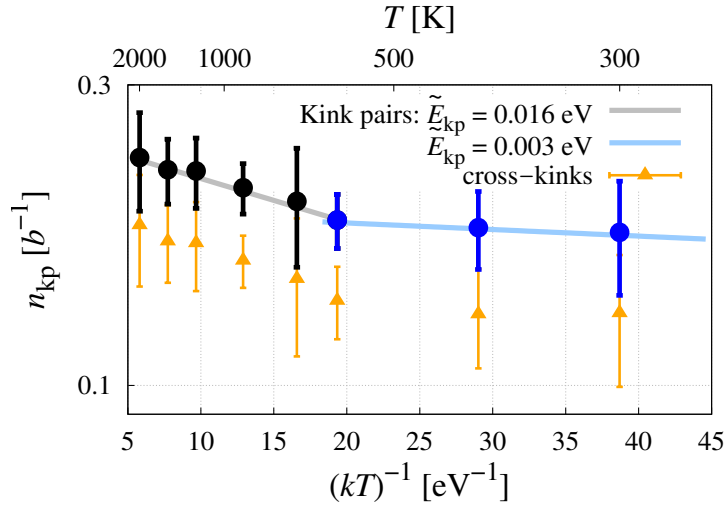


Figure 3.3: Equilibrium concentration of kink pairs and cross-kinks per unit length in Burgers vector units as a function of (inverse) temperature. Two regimes can be clearly appreciated, each characterized by Arrhenius fits with energies of 0.003 and 0.016 eV at low and high temperatures, respectively. Orange dots represent the equilibrium concentration of cross-kinks as a function of T . Error bars are representative of the standard variation obtained from 10 independent simulations at each temperature.

Two temperature regimes can be clearly distinguished in the figure. At low T (blue markers), the data points follow an Arrhenius expression with an activation energy of $\tilde{E} = 0.003$ eV, while at high temperatures (black dots), the best fit is given by an activation energy of 0.016 eV. This contrasts with the kink-pair activation energies for the pure substances and the average alloy given in Table 3.1, which are over one order of magnitude larger. Error bars reflect the variability across the 10 independent cases. The first important implication of these results is that kink pairs and cross-kinks may form practically spontaneously at all temperatures (as indicated by the very low effective formation energies, \tilde{E}). In practical terms, this removes kink-pair nucleation as the rate-limiting step in screw dislocation motion, shifting it instead to lateral kink propagation and cross-kink dissolution. Second, kinks and cross-kinks are seen to exist on multiple glide planes, often in opposite directions relative to the original dislocation line. For this reason the dislocation predisposes itself to resist motion by glide irrespective of the direction of such motion, i.e., regardless of where the maximum RSS is applied. In other words, the glide stress must be sufficiently high to untangle the dislocation line from features spread on non-glide planes in its ground state. This confers an intrinsic strength to screw dislocation lines not found in their pure metal counterparts.

3.3.2 Velocity-stress relations

Next, we investigate the temperature dependence of the alloy strength using the line configurations obtained above as the starting structures for the kMC simulations. Stress is applied on a primary (110) plane (i.e., the MRSS plane) and the velocity of the dislocation's center of mass is measured from the resulting displacement-time relations. The results are plotted in Figure 3.4 at five different temperatures.

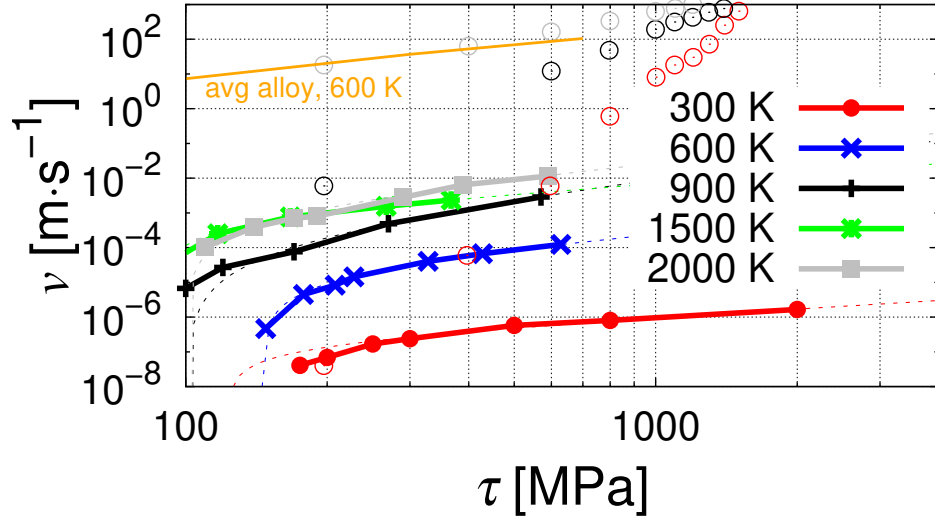


Figure 3.4: Mean screw dislocation velocity as a function of resolved shear stress and temperature for $500b$ dislocation lines. Dashed lines represent best fits to power laws of the type: $v(\tau) = a(\tau - \tau_{s-p})^m$. Open circles correspond to simulations in pure W under the same conditions at 300 and 900 K. Pure W simulations follow a perfect exponential velocity-stress dependence, with no threshold stress at any temperature. The orange curve corresponds to the ‘average’ Nb-Mo-Ta-W alloy at 600 K.

As the figure shows, a threshold stress is required to overcome the static self-pinning effect at each temperature. This stress, denoted by τ_{s-p} , is the manifestation of the hardening associated with the equilibrium line configurations. Additionally, a strong dynamic hardening effect arises from the formation of ‘debris’ loops during dislocation glide¹. An example is given in Figure 3.2b, which shows the instantaneous line configuration during dislocation motion at 900 K and 800 MPa. Dynamic hardening is defined by a proportionality constant a that modulates the effect of the glide stress on the dislocation velocity. τ_{s-p} and a are

¹This distinction between static and dynamic threshold stresses was first proposed by Rodary et al. [163] for Ni-Al alloys.

obtained from power law fits to the data for each temperature of the expression:

$$v(\tau) = a(\tau - \tau_{s-p})^m, \quad \text{when } \tau > \tau_{s-p} \quad (3.4)$$

The parameters associated with each fit that give the velocity in meters per second are given in Table 3.2. These curves are shown as colored dashed lines in Fig. 3.4. As Table

Table 3.2: Parameters of the power fits shown in Figure 3.4 according to eq. 3.4.

T [K]	a	m	τ_{s-p} [MPa]
300	4.40×10^{-9}	0.79	123
600	7.80×10^{-8}	1.19	145
900	5.80×10^{-8}	1.76	100
1500	1.41×10^{-5}	0.91	90
2000	2.55×10^{-6}	1.36	100

3.2 shows, m hovers around unity, well below the exponential scaling typically seen in pure bcc metals [158, 164] (which has been added to the figure for pure W as a comparison). As discussed earlier, τ_{s-p} is directly related to the starting dislocation configuration, which includes an intrinsic concentration of kinks and cross-kinks. This concentration increases with temperature as indicated by the values given in Fig. 3.3. However, the combined effect of stress and temperature helps ‘undo’ the existing kink pairs and cross-kinks on planes different than the MRSSP. Thus, a competition between strengthening due to a high concentration of steps on the line and a softening effect due to the undoing of these steps ensues. The exception to this behavior is at 0 K, for which $n_{kp} = 0$ and lines are perfectly straight and therefore $\tau_{s-p} = 0$.

3.3.3 Temperature dependence of the dislocation critical stress

To obtain the total critical stress for screw dislocation motion as a function of temperature, we follow the procedure used in ref. [155] and extract the stress at which the resulting shear rate is 10^{-4} s^{-1} (typical laboratory strain rate). For this, we use Orowan's equation assuming a dislocation density of $\rho_d = 10^{14} \text{ m}^{-2}$, $\dot{\epsilon} = b\rho_d v(\tau)$. The critical stress at each temperature, $\tau^*(T)$, is thus obtained as that at which the velocity is equal to $v(\tau^*) = \dot{\epsilon}/b\rho_d$, and consists of thermal and self-pinning contributions. As mentioned earlier, 0 K is the only instance in which the self-pinning stress is equal to zero. The resulting τ^*-T dependence is shown in Figure 3.5. At low temperatures, the thermal component of τ^* is dominant, as

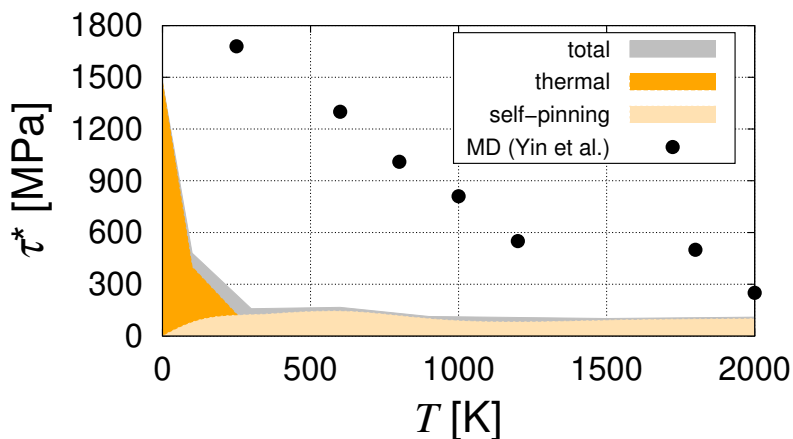


Figure 3.5: Temperature dependence of the critical stress for screw dislocation motion. The total stress results from the additive effects of the thermal stress (due to thermally-activated processes), and the self-pinning stress (due to the intrinsic line roughness under zero applied stress conditions). Black dots correspond to MD results of the critical (threshold) stress from ref. [1].

dislocation motion becomes controlled by kink propagation and de-pinning, both of which display a strong temperature dependence. Thereafter, the thermal stress drops abruptly with temperature and is overtaken by the self-pinning stress. This is mostly due to cross-kink dissolution, which is a process unique to refractory multicomponent alloys such as the

present one [146, 156, 165, 166]. The self-pinning stress increases modestly from its value of zero at 0 K to its peak of 145 MPa at 600 K. It subsequently hovers around 100 MPa due to the dual temperature effect of favoring higher concentrations of thermal kinks/cross-kinks (see Fig. 3.3) as well as facilitating their ‘undoing’.

τ^* represents the critical resolved shear stress for dislocation motion and is thus a *static* threshold stress that must be overcome before dislocation motion can be initiated. As indicated above, however, once dislocation motion begins, a dynamic self-hardening effect sets in, which results in pronounced line roughness and production of ‘debris’ loops of prismatic character. Dynamic hardening is only limited by line topology and it can thus potentially occur in pure metals, although only at very high strain rates and temperatures [153, 167]. Conversely, in RMEA it can take place at quasistatic deformation rates and room temperature or below [156, 168], which is one of the reasons why bcc multi-principal element alloys are always stronger at low temperatures than any of its pure element constituents, including the ‘average’ alloy (a fictitious pure metal whose properties are equal to the compositional average of the individual element properties in the alloy). This behavior is consistent with our previous study in Nb-Ta-V alloys [156], as is for Nb-Mo-Ta-W, demonstrated in Fig. 3.4 by the higher velocity of the average alloy at 600 K compared to the alloy.

3.4 Discussion

Our simulations indicate that the contribution of screw dislocations to the strength of Nb-Mo-Ta-W alloys is only significant below room temperature. While this is consistent with the standard picture of bcc metal plasticity, a nonstandard contribution in the form of a constant remnant value of 100 MPa up to 2000 K is also observed. This is due to special features that are unique to high-entropy alloys, namely, the role of compositional fluctuations in eliminating the need for thermal activation at low temperatures as the driver for dislocation glide. However, a collateral effect of such compositional complexity is the onset of line

roughness. In turn, this gives rise to a ‘baseline’ strength associated with the almost athermal existence of kinks and cross-kinks spread over multiple nonparallel glide planes. As stress is applied to move the dislocation along a given direction, the applied stress first has to overcome this intrinsic strengthening by undoing all these features.

It is worth noting that our kMC model works with random atomistic environments, mostly representative of random solid solutions. So we do not discount additional strengthening effects associated with the onset of atomic order in the lattice, as it has been seen in several other RMEA [1, 52, 146]. Likewise, the present model does not capture ‘hierarchical’ energy landscapes, i.e., those characterized with energy minima at several length scales [169, 170]. As such, the energy barriers considered in this study belong to atomic-level transitions only. These transitions take place over a configurational landscape governed by lattice distortions. In fact, to investigate the role that lattice distortion plays on static and dynamic strengthening during dislocation glide, we have conducted a preliminary study of dislocation dynamics in the equiatomic binaries Nb-Ta (similar a_0) and Nb-W (dissimilar a_0) systems, noting that even a reduced lattice parameter mismatch is still sufficient to induce changes conducive to extra strength relative to a pure system.

In terms of comparison with MD simulations, the results by Yin et al. [1] include detailed velocity-stress relations for the random equiatomic Nb-Mo-Ta-W system using the same interatomic potential employed in this work. However, the velocities obtained by MD are almost four orders of magnitude higher than those predicted with kMC. The differences that might contribute to such large differences have been amply discussed in the literature [158, 171–173], and can be attributed to MD’s inability to probe dislocation lines sufficiently long to develop the kind of stress-free configurations obtained here. Interestingly, however, the general dependence of the dislocation velocity on stress is quite similar in both cases (quasi-linear). As well, the threshold stresses obtained by MD simulations –added as black dots for comparison in Fig. 3.5– are substantially larger than those computed here.

Finally, in light of the inability of screw dislocations to provide strength at medium and

high temperatures, the attention is turning to edge dislocations, whose role in RMEA plasticity is being actively investigated [174–178]. Indeed, a comprehensive model of refractory multielement alloys in the entire temperature range must include both contributions, which is the subject of ongoing work by the authors as well.

3.5 Conclusions

To summarize this chapter, we have extended a kinetic Monte Carlo model of thermally activated screw dislocation kinetics to equiatomic Nb-Mo-Ta-W alloys. The model calculates all the necessary interaction energies from the local atomistic environment around the dislocation line, using values obtained *a priori* from data-fitted interatomic potentials. Compositional fluctuations lead to high concentrations of kink pairs and cross-kinks (defined by formation energies of only a few meV). This leads to highly-tortuous equilibrium line configurations characterized by the presence of kinks and cross-kinks spread over multiple slip planes, effectively pinning the line prior to the application of glide stress. The key to the strengthening mechanism observed in our simulations is the balance of two competing processes: (i) a strengthening effect due to the existence of thermal kinks and cross-kinks in equilibrium, and (ii) a softening effect driven by cross-kink annihilation. Both of these are enhanced as temperature increases, resulting in a baseline strength of ≈ 100 MPa that extends up to 2000 K. Finally, dislocation velocities are seen to display power law type dependencies with applied stress. These laws are defined by exponents close to unity, signifying a marked departure from the exponential dependence observed in pure bcc metals.

Bibliography

- [1] S. Yin, Y. Zuo, A. Abu-Odeh, H. Zheng, X.-G. Li, J. Ding, S. P. Ong, M. Asta, R. O. Ritchie, Atomistic simulations of dislocation mobility in refractory high-entropy alloys and the effect of chemical short-range order, *Nature communications* 12 (1) (2021) 1–14.
- [2] L. Dezerald, L. Proville, L. Ventelon, F. Willaime, D. Rodney, First-principles prediction of kink-pair activation enthalpy on screw dislocations in bcc transition metals: V, Nb, Ta, Mo, W, and Fe, *Physical Review B* 91 (9) (2015) 094105.
- [3] B. Cantor, I. Chang, P. Knight, A. Vincent, Microstructural development in equiatomic multicomponent alloys, *Materials Science and Engineering: A* 375-377 (2004) 213 – 218. doi:<https://doi.org/10.1016/j.msea.2003.10.257>.
URL <http://www.sciencedirect.com/science/article/pii/S0921509303009936>
- [4] J.-W. Yeh, S.-K. Chen, S.-J. Lin, J.-Y. Gan, T.-S. Chin, T.-T. Shun, C.-H. Tsau, S.-Y. Chang, Nanostructured high-entropy alloys with multiple principal elements: Novel alloy design concepts and outcomes, *Advanced Engineering Materials* 6 (5) 299–303. arXiv:<https://onlinelibrary.wiley.com/doi/pdf/10.1002/adem.200300567>, doi:10.1002/adem.200300567.
URL <https://onlinelibrary.wiley.com/doi/abs/10.1002/adem.200300567>
- [5] R. Kozak, A. Sologubenko, W. Steurer, Single-phase high-entropy alloys: an overview, *Zeitschrift für Kristallographie - Crystalline Materials* 230 (1) (2015) 55 – 68. doi:<https://doi.org/10.1515/zkri-2014-1739>.
URL <https://www.degruyter.com/view/journals/zkri/230/1/article-p55.xml>
- [6] High-Entropy Alloys: Formation and Properties, Vol. ASME 2018 Symposium on Elevated Temperature Application of Materials for Fossil, Nuclear, and Petrochemical Industries of Pressure Technology, v001T01A004.

arXiv:<https://asmedigitalcollection.asme.org/PT/proceedings-pdf/ETAM2018/40764/V001T01A004/2381193/v001t01a004-etam2018-6732.pdf>,
doi:10.1115/ETAM2018-6732.

URL <https://doi.org/10.1115/ETAM2018-6732>

- [7] O. Senkov, J. Miller, D. Miracle, C. Woodward, Accelerated exploration of multi-principal element alloys for structural applications, *Calphad* 50 (2015) 32–48.
- [8] Z. Li, K. G. Pradeep, Y. Deng, D. Raabe, C. C. Tasan, Metastable high-entropy dual-phase alloys overcome the strength–ductility trade-off, *Nature* 534 (7606) (2016) 227–230.
- [9] D. Miracle, O. Senkov, A critical review of high entropy alloys and related concepts, *Acta Materialia* 122 (2017) 448 – 511. doi:<https://doi.org/10.1016/j.actamat.2016.08.081>.
URL <http://www.sciencedirect.com/science/article/pii/S1359645416306759>
- [10] M.-H. Tsai, J.-W. Yeh, High-entropy alloys: A critical review, *Materials Research Letters* 2 (3) (2014) 107–123. arXiv:<https://doi.org/10.1080/21663831.2014.912690>, doi:10.1080/21663831.2014.912690.
URL <https://doi.org/10.1080/21663831.2014.912690>
- [11] S.-q. Xia, W. Zhen, T.-f. Yang, Y. Zhang, Irradiation behavior in high entropy alloys, *Journal of Iron and Steel Research, International* 22 (10) (2015) 879–884.
- [12] S. Xia, M. C. Gao, T. Yang, P. K. Liaw, Y. Zhang, Phase stability and microstructures of high entropy alloys ion irradiated to high doses, *Journal of Nuclear Materials* 480 (2016) 100–108.
- [13] N. K. Kumar, C. Li, K. Leonard, H. Bei, S. Zinkle, Microstructural stability and mechanical behavior of fenimnrcr high entropy alloy under ion irradiation, *Acta Materialia* 113 (2016) 230–244.

- [14] T. Egami, W. Guo, P. Rack, T. Nagase, Irradiation resistance of multicomponent alloys, *Metallurgical and Materials Transactions A* 45 (1) (2014) 180–183.
- [15] O. Senkov, S. Senkova, C. Woodward, Effect of aluminum on the microstructure and properties of two refractory high-entropy alloys, *Acta Materialia* 68 (2014) 214–228. doi:[10.1016/j.actamat.2014.01.029](https://doi.org/10.1016/j.actamat.2014.01.029).
- [16] O. Senkov, G. Wilks, J. Scott, D. Miracle, Mechanical properties of $\text{Nb}_{25}\text{Mo}_{25}\text{Ta}_{25}\text{W}_{25}$ and $\text{V}_{20}\text{Nb}_{20}\text{Mo}_{20}\text{Ta}_{20}\text{W}_{20}$ refractory high entropy alloys, *Intermetallics* 19 (5) (2011) 698 – 706. doi:<https://doi.org/10.1016/j.intermet.2011.01.004>.
URL <http://www.sciencedirect.com/science/article/pii/S0966979511000185>
- [17] C.-C. Juan, M.-H. Tsai, C.-W. Tsai, C.-M. Lin, W.-R. Wang, C.-C. Yang, S.-K. Chen, S.-J. Lin, J.-W. Yeh, Enhanced mechanical properties of hfmotatizr and hfmonbtatizr refractory high-entropy alloys, *Intermetallics* 62 (2015) 76–83.
- [18] O. Senkov, C. Woodward, D. Miracle, Microstructure and properties of aluminum-containing refractory high-entropy alloys, *Jom* 66 (2014) 2030–2042.
- [19] M. S. Rizi, H. Minouei, B. J. Lee, H. Pouraliakbar, M. R. Toroghinejad, S. I. Hong, Hierarchically activated deformation mechanisms to form ultra-fine grain microstructure in carbon containing femncocr twinning induced plasticity high entropy alloy, *Materials Science and Engineering: A* 824 (2021) 141803. doi:<https://doi.org/10.1016/j.msea.2021.141803>.
URL <https://www.sciencedirect.com/science/article/pii/S0921509321010698>
- [20] S. H. Shim, H. Pouraliakbar, S. I. Hong, High strength dual fcc phase cocufemni high-entropy alloy wires with dislocation wall boundaries stabilized by phase boundaries, *Materials Science and Engineering: A* 825 (2021) 141875. doi:<https://doi.org/10.1016/j.msea.2021.141875>.

URL <https://www.sciencedirect.com/science/article/pii/S0921509321011412>

- [21] O. Senkov, G. Wilks, D. Miracle, C. Chuang, P. Liaw, Refractory high-entropy alloys, *Intermetallics* 18 (9) (2010) 1758 – 1765. doi:<https://doi.org/10.1016/j.intermet.2010.05.014>.

URL <http://www.sciencedirect.com/science/article/pii/S0966979510002475>

- [22] Y. Zou, S. Maiti, W. Steurer, R. Spolenak, Size-dependent plasticity in an $\text{nb}_{25}\text{mo}_{25}\text{ta}_{25}\text{w}_{25}$ refractory high-entropy alloy, *Acta Materialia* 65 (2014) 85 – 97. doi:<https://doi.org/10.1016/j.actamat.2013.11.049>.

URL <http://www.sciencedirect.com/science/article/pii/S1359645413009075>

- [23] H. Yao, J.-W. Qiao, M. C. Gao, J. A. Hawk, S.-G. Ma, H. Zhou, Monbtav medium-entropy alloy, *Entropy* 18 (5) (2016). doi:[10.3390/e18050189](https://doi.org/10.3390/e18050189).

URL <https://www.mdpi.com/1099-4300/18/5/189>

- [24] F. Körmann, M. H. Sluiter, Interplay between lattice distortions, vibrations and phase stability in nbmotaw high entropy alloys, *Entropy* 18 (8) (2016). doi:[10.3390/e18080403](https://doi.org/10.3390/e18080403).

URL <https://www.mdpi.com/1099-4300/18/8/403>

- [25] H. Yao, J. Qiao, J. Hawk, H. Zhou, M. Chen, M. Gao, Mechanical properties of refractory high-entropy alloys: Experiments and modeling, *Journal of Alloys and Compounds* 696 (2017) 1139 – 1150. doi:<https://doi.org/10.1016/j.jallcom.2016.11.188>.

URL <http://www.sciencedirect.com/science/article/pii/S0925838816336647>

- [26] H. Dobbstein, M. Thiele, E. L. Gurevich, E. P. George, A. Ostendorf, Direct metal deposition of refractory high entropy alloy monbtaw , *Physics Procedia* 83 (2016) 624 – 633, laser Assisted Net Shape Engineering 9 International Conference on Photonic

Technologies Proceedings of the LANE 2016 September 19-22, 2016 FÃ¼rth, Germany.
doi:<https://doi.org/10.1016/j.phpro.2016.08.065>.

URL <http://www.sciencedirect.com/science/article/pii/S1875389216301729>

- [27] S. A. Kube, S. Sohn, D. Uhl, A. Datye, A. Mehta, J. Schroers, Phase selection motifs in high entropy alloys revealed through combinatorial methods: Large atomic size difference favors bcc over fcc, *Acta Materialia* 166 (2019) 677 – 686. doi:<https://doi.org/10.1016/j.actamat.2019.01.023>.

URL <http://www.sciencedirect.com/science/article/pii/S1359645419300382>

- [28] Q. Xu, H. Guan, Z. Zhong, S. Huang, J. Zhao, Irradiation resistance mechanism of the cocrfemni equiatomic high-entropy alloy, *Scientific Reports* 11 (1) (2021) 608.

- [29] W. Chen, X. Ding, Y. Feng, X. Liu, K. Liu, Z. Lu, D. Li, Y. Li, C. Liu, X.-Q. Chen, Vacancy formation enthalpies of high-entropy fecorni alloy via first-principles calculations and possible implications to its superior radiation tolerance, *Journal of Materials Science Technology* 34 (2) (2018) 355–364. doi:<https://doi.org/10.1016/j.jmst.2017.11.005>.

URL <https://www.sciencedirect.com/science/article/pii/S1005030217302670>

- [30] S. W. McAlpine, J. V. Logan, M. P. Short, Predicting single phase stability and segregation in the nbmotati-(w, v) high entropy alloy system with the vacancy exchange potential, *Scripta Materialia* 191 (2021) 29–33.

- [31] 3 - dislocation motion at elevated temperatures, in: J.-S. Zhang (Ed.), *High Temperature Deformation and Fracture of Materials*, Woodhead Publishing, 2010, pp. 28 – 39. doi:<https://doi.org/10.1533/9780857090805.1.28>.

URL <http://www.sciencedirect.com/science/article/pii/B9780857090799500033>

- [32] A. Roy, J. Munshi, G. Balasubramanian, Low energy atomic traps sluggish the diffusion in compositionally complex refractory alloys, *Intermetallics* 131 (2021) 107106. doi:<https://doi.org/10.1016/j.intermet.2021.107106>.
URL <https://www.sciencedirect.com/science/article/pii/S0966979521000236>
- [33] Y.-C. Huang, Y.-C. Lai, Y.-H. Lin, S.-K. Wu, A study on the severely cold-rolled and annealed quaternary equiatomic derivatives from quinary hfnbtatizr refractory high entropy alloy, *Journal of Alloys and Compounds* 855 (2021) 157404. doi:<https://doi.org/10.1016/j.jallcom.2020.157404>.
URL <https://www.sciencedirect.com/science/article/pii/S0925838820337683>
- [34] P. Cao, H. Huang, S. Jiang, X. Liu, H. Wang, Y. Wu, Z. Lu, Microstructural stability and aging behavior of refractory high entropy alloys at intermediate temperatures, *Journal of Materials Science & Technology* 122 (2022) 243–254.
- [35] E. Antillon, C. Woodward, S. Rao, B. Akdim, T. Parthasarathy, Chemical short range order strengthening in a model fcc high entropy alloy, *Acta Materialia* 190 (2020) 29–42.
- [36] E. Ma, Unusual dislocation behavior in high-entropy alloys, *Scripta Materialia* 181 (2020) 127–133.
- [37] C. Lu, T. Yang, K. Jin, N. Gao, P. Xiu, Y. Zhang, F. Gao, H. Bei, W. J. Weber, K. Sun, et al., Radiation-induced segregation on defect clusters in single-phase concentrated solid-solution alloys, *Acta Materialia* 127 (2017) 98–107.
- [38] K. Jin, B. C. Sales, G. M. Stocks, G. D. Samolyuk, M. Daene, W. J. Weber, Y. Zhang, H. Bei, Tailoring the physical properties of ni-based single-phase equiatomic alloys by modifying the chemical complexity, *Scientific reports* 6 (1) (2016) 20159.

- [39] B. C. Sales, K. Jin, H. Bei, G. M. Stocks, G. D. Samolyuk, A. F. May, M. A. McGuire, Quantum critical behavior in a concentrated ternary solid solution, *Scientific reports* 6 (1) (2016) 26179.
- [40] P. Tulip, J. B. Staunton, S. Lowitzer, D. Koedderitzsch, H. Ebert, Theory of electronic transport in random alloys with short-range order: Korringa-kohn-rostoker nonlocal coherent potential approximation, *Physical Review B* 77 (16) (2008) 165116.
- [41] Z. Shen, J.-P. Du, S. Shinzato, Y. Sato, P. Yu, S. Ogata, Kinetic monte carlo simulation framework for chemical short-range order formation kinetics in a multi-principal-element alloy, *Computational Materials Science* 198 (2021) 110670.
- [42] S. Zhao, Role of chemical disorder and local ordering on defect evolution in high-entropy alloys, *Phys. Rev. Materials* 5 (2021) 103604. doi:10.1103/PhysRevMaterials.5.103604.
URL <https://link.aps.org/doi/10.1103/PhysRevMaterials.5.103604>
- [43] S. Zhao, Effects of local elemental ordering on defect-grain boundary interactions in high-entropy alloys, *Journal of Alloys and Compounds* 887 (2021) 161314.
- [44] C. M. Barr, J. E. Nathaniel II, K. A. Unocic, J. Liu, Y. Zhang, Y. Wang, M. L. Taheri, Exploring radiation induced segregation mechanisms at grain boundaries in equiatomic cocrfenimn high entropy alloy under heavy ion irradiation, *Scripta Materialia* 156 (2018) 80–84.
- [45] A. Esfandiarpour, M. Nasrabadi, Vacancy formation energy in cunico equimolar alloy and cunico high entropy alloy: ab initio based study, *Calphad* 66 (2019) 101634.
- [46] X. Zhang, S. V. Divinski, B. Grabowski, Ab initio prediction of vacancy energetics in hcp al-hf-sc-ti-zr high entropy alloys and the subsystems, *Acta Materialia* 227 (2022) 117677.

- [47] C. Li, J. Yin, K. Odbadrakh, B. C. Sales, S. J. Zinkle, G. M. Stocks, B. D. Wirth, First principle study of magnetism and vacancy energetics in a near equimolar nifemncr high entropy alloy, *Journal of Applied Physics* 125 (15) (2019).
- [48] B. Xing, X. Wang, W. J. Bowman, P. Cao, Short-range order localizing diffusion in multi-principal element alloys, *Scripta Materialia* 210 (2022) 114450.
- [49] S. Zhao, Defect properties in a vtacrw equiatomic high entropy alloy (hea) with the body centered cubic (bcc) structure, *Journal of Materials Science & Technology* 44 (2020) 133–139.
- [50] L. Nibbelink, *Simulating Vacancy Formation and Diffusion in NbMoTaW*, University of California, San Diego, 2020.
- [51] A. P. Thompson, H. M. Aktulga, R. Berger, D. S. Bolintineanu, W. M. Brown, P. S. Crozier, P. J. in't Veld, A. Kohlmeyer, S. G. Moore, T. D. Nguyen, et al., Lammmps-a flexible simulation tool for particle-based materials modeling at the atomic, meso, and continuum scales, *Computer Physics Communications* 271 (2022) 108171.
- [52] X.-G. Li, C. Chen, H. Zheng, Y. Zuo, S. P. Ong, Complex strengthening mechanisms in the nbmotaw multi-principal element alloy, *npj Computational Materials* 6 (1) (2020) 1–10.
- [53] A. Stukowski, Visualization and analysis of atomistic simulation data with ovito—the open visualization tool, *Modelling and Simulation in Materials Science and Engineering* 18 (1) (2009) 015012.
- [54] D. de Fontaine, The number of independent pair-correlation functions in multicomponent systems, *Journal of Applied Crystallography* 4 (1) (1971) 15–19.
- [55] A. Fernández-Caballero, J. S. Wróbel, P. M. Mummery, D. Nguyen-Manh, Short-range

- order in high entropy alloys: Theoretical formulation and application to mo-nb-ta-v-w system, *Journal of Phase Equilibria and Diffusion* 38 (4) (2017) 391–403.
- [56] J. Byggmästar, K. Nordlund, F. Djurabekova, Modeling refractory high-entropy alloys with efficient machine-learned interatomic potentials: Defects and segregation, *Physical Review B* 104 (10) (2021) 104101.
- [57] M. Hossain, J. Marian, Stress-dependent solute energetics in w–re alloys from first-principles calculations, *Acta Materialia* 80 (2014) 107–117.
- [58] K. Sugita, N. Matsuoka, M. Mizuno, H. Araki, Vacancy formation enthalpy in cocr-femni high-entropy alloy, *Scripta Materialia* 176 (2020) 32–35.
- [59] E.-W. Huang, H.-S. Chou, K. Tu, W.-S. Hung, T.-N. Lam, C.-W. Tsai, C.-Y. Chiang, B.-H. Lin, A.-C. Yeh, S.-H. Chang, et al., Element effects on high-entropy alloy vacancy and heterogeneous lattice distortion subjected to quasi-equilibrium heating, *Scientific reports* 9 (1) (2019) 14788.
- [60] R. R. Eleti, T. Bhattacharjee, A. Shibata, N. Tsuji, Unique deformation behavior and microstructure evolution in high temperature processing of hfnbtatizr refractory high entropy alloy, *Acta Materialia* 171 (2019) 132–145.
- [61] Q. Liu, G. Wang, Y. Liu, X. Sui, Y. Chen, S. Luo, Hot deformation behaviors of an ultrafine-grained monbtativ refractory high-entropy alloy fabricated by powder metallurgy, *Materials Science and Engineering: A* 809 (2021) 140922.
- [62] T. Prohaska, J. Irrgeher, J. Benefield, J. K. Böhlke, L. A. Chesson, T. B. Coplen, T. Ding, P. J. Dunn, M. Gröning, N. E. Holden, et al., Standard atomic weights of the elements 2021 (iupac technical report), *Pure and Applied Chemistry* 94 (5) (2022) 573–600.

- [63] S. Zhao, Y. Xiong, S. Ma, J. Zhang, B. Xu, J.-J. Kai, Defect accumulation and evolution in refractory multi-principal element alloys, *Acta Materialia* 219 (2021) 117233.
- [64] A. Roy, P. Singh, G. Balasubramanian, D. D. Johnson, Vacancy formation energies and migration barriers in multi-principal element alloys, *Acta Materialia* 226 (2022) 117611.
- [65] Z. Wang, C. Liu, P. Dou, Thermodynamics of vacancies and clusters in high-entropy alloys, *Physical Review Materials* 1 (4) (2017) 043601.
- [66] O. N. Senkov, D. B. Miracle, K. J. Chaput, J.-P. Couzinie, Development and exploration of refractory high entropy alloys? a review, *Journal of Materials Research* 33 (19) (2018) 3092–3128. doi:10.1557/jmr.2018.153.
- [67] J.-W. Yeh, S.-J. Lin, Breakthrough applications of high-entropy materials, *Journal of Materials Research* 33 (19) (2018) 3129–3137. doi:10.1557/jmr.2018.283.
- [68] D. B. Miracle, J. D. Miller, O. N. Senkov, C. Woodward, M. D. Uchic, J. Tiley, Exploration and development of high entropy alloys for structural applications, *Entropy* 16 (1) (2014) 494–525. doi:10.3390/e16010494.
URL <https://www.mdpi.com/1099-4300/16/1/494>
- [69] M. Wang, Z. Ma, Z. Xu, X. Cheng, Designing vxnbmota refractory high-entropy alloys with improved properties for high-temperature applications, *Scripta Materialia* 191 (2021) 131–136.
- [70] M. Cusentino, M. Wood, R. Dingreville, Compositional and structural origins of radiation damage mitigation in high-entropy alloys, *Journal of Applied Physics* 128 (12) (2020).
- [71] A. Lin-Vines, J. Wilson, A. Fraile, L. J. Evitts, M. Rushton, J. Astbury, W. Lee, S. C.

- Middleburgh, Defect behaviour in the monbtavw high entropy alloy (hea), *Results in Materials* 15 (2022) 100320.
- [72] O. El-Atwani, N. Li, M. Li, A. Devaraj, J. Baldwin, M. M. Schneider, D. Sobieraj, J. S. Wróbel, D. Nguyen-Manh, S. A. Maloy, et al., Outstanding radiation resistance of tungsten-based high-entropy alloys, *Science advances* 5 (3) (2019) eaav2002.
- [73] Q. Xu, H. Guan, S. Huang, Z. Zhong, H. Watanabe, M. Tokitani, Compositional stability in medium and high-entropy alloys of cocrfemnni system under ion irradiation, *Journal of Alloys and Compounds* 925 (2022) 166697.
- [74] Z. Su, J. Ding, M. Song, L. Jiang, T. Shi, Z. Li, S. Wang, F. Gao, D. Yun, E. Ma, et al., Enhancing the radiation tolerance of high-entropy alloys via solute-promoted chemical heterogeneities, *Acta Materialia* 245 (2023) 118662.
- [75] Z. Cheng, J. Sun, X. Gao, Y. Wang, J. Cui, T. Wang, H. Chang, Irradiation effects in high-entropy alloys and their applications, *Journal of Alloys and Compounds* 930 (2023) 166768.
- [76] H. Li, L. Zhao, H. Zong, X. Ding, et al., Improving radiation-tolerance of bcc multi-principal element alloys by tailoring compositional heterogeneities, *Journal of Nuclear Materials* 555 (2021) 153140.
- [77] G. Was, *Irradiation Creep and Growth*, Springer Berlin Heidelberg, Berlin, Heidelberg, 2007, pp. 711–763.
- [78] G. Odette, Modeling of microstructural evolution under irradiation, *Journal of Nuclear Materials* 85 (1979) 533–545.
- [79] M. Kiritani, Microstructure evolution during irradiation, *Journal of Nuclear materials* 216 (1994) 220–264.

- [80] B. Wirth, G. Odette, D. Maroudas, G. Lucas, Energetics of formation and migration of self-interstitials and self-interstitial clusters in α -iron, *Journal of nuclear materials* 244 (3) (1997) 185–194.
- [81] S. J. Zinkle, G. Was, Materials challenges in nuclear energy, *Acta Materialia* 61 (3) (2013) 735–758.
- [82] Q. Yu, G. Po, J. Marian, Physics-based model of irradiation creep for ferritic materials under fusion energy operation conditions, *Journal of applied physics* 132 (22) (2022).
- [83] B. Wirth, G. Odette, D. Maroudas, G. Lucas, Dislocation loop structure, energy and mobility of self-interstitial atom clusters in bcc iron, *Journal of nuclear materials* 276 (1-3) (2000) 33–40.
- [84] A. Barashev, Y. N. Osetsky, D. Bacon, Mechanism of one-dimensional glide of self-interstitial atom clusters in α -iron, *Philosophical Magazine A* 80 (11) (2000) 2709–2720.
- [85] Y. N. Osetsky, D. Bacon, A. Serra, B. Singh, S. Golubov, Stability and mobility of defect clusters and dislocation loops in metals, *Journal of nuclear materials* 276 (1-3) (2000) 65–77.
- [86] N. Soneda, T. Diaz de La Rubia, Migration kinetics of the self-interstitial atom and its clusters in bcc fe, *Philosophical Magazine A* 81 (2) (2001) 331–343.
- [87] J. Marian, B. Wirth, A. Caro, B. Sadigh, G. Odette, J. Perlado, T. D. de la Rubia, Dynamics of self-interstitial cluster migration in pure α -fe and fe-cu alloys, *Physical review B* 65 (14) (2002) 144102.
- [88] N. Anento, A. Serra, Y. N. Osetsky, Atomistic study of multimechanism diffusion by self-interstitial defects in α -fe, *Modelling and Simulation in Materials Science and Engineering* 18 (2) (2010) 025008.

- [89] D. Terentyev, L. Malerba, M. Hou, Dimensionality of interstitial cluster motion in bcc-fe, *Physical Review B* 75 (10) (2007) 104108.
- [90] M. Hatanaka, E. Kuramoto, K. Ono, H. Mori, Changes in the burgers vector of perfect dislocation loops without contact with the external dislocations, *Physical review letters* 96 (12) (2006) 125506.
- [91] L. Gharaee, J. Marian, P. Erhart, The role of interstitial binding in radiation induced segregation in w-re alloys, *Journal of Applied Physics* 120 (2) (2016).
- [92] C.-H. Huang, L. Gharaee, Y. Zhao, P. Erhart, J. Marian, Mechanism of nucleation and incipient growth of re clusters in irradiated w-re alloys from kinetic monte carlo simulations, *Physical Review B* 96 (9) (2017) 094108.
- [93] Y. Xiong, J. Zhang, S. Ma, S. Huang, B. Xu, S. Zhao, Multiscale modeling of irradiation-induced defect evolution in bcc multi principal element alloys, *Journal of Alloys and Compounds* 953 (2023) 170084.
- [94] C.-C. Fu, F. Willaime, P. Ordejón, Stability and mobility of mono-and di-interstitials in α -fe, *Physical review letters* 92 (17) (2004) 175503.
- [95] J. Marian, B. Wirth, G. Odette, J. Perlado, Cu diffusion in α -fe: determination of solute diffusivities using atomic-scale simulations, *Computational materials science* 31 (3-4) (2004) 347–367.
- [96] L. A. Zepeda-Ruiz, J. Rottler, B. D. Wirth, R. Car, D. J. Srolovitz, Self-interstitial transport in vanadium, *Acta materialia* 53 (7) (2005) 1985–1994.
- [97] K. Ono, K. Mimura, M. Uchikoshi, H. Mori, Observation of the one-dimensional diffusion of nanometer-sized dislocation loops, *Science* 318 (5852) (2007) 956–959.

- [98] C. Becquart, R. N. Happy, P. Olsson, C. Domain, A dft study of the stability of sias and small sia clusters in the vicinity of solute atoms in fe, *Journal of Nuclear Materials* 500 (2018) 92–109.
- [99] D. Nguyen-Manh, A. Horsfield, S. Dudarev, Self-interstitial atom defects in bcc transition metals: Group-specific trends, *Physical Review B* 73 (2) (2006) 020101.
- [100] R. Alexander, M.-C. Marinica, L. Proville, F. Willaime, K. Arakawa, M. Gilbert, S. Dudarev, Ab initio scaling laws for the formation energy of nanosized interstitial defect clusters in iron, tungsten, and vanadium, *Physical Review B* 94 (2) (2016) 024103.
- [101] Y.-P. Zhao, Y.-K. Dou, X.-F. He, H.-q. Deng, L.-f. Wang, W. Yang, An atomic scale study on self-interstitial formation and diffusion behaviors in tivta and tivtanb concentrated solid-solution alloys, *Computational Materials Science* 218 (2023) 111943.
- [102] J. Byggmästar, K. Nordlund, F. Djurabekova, Simple machine-learned interatomic potentials for complex alloys, *Physical Review Materials* 6 (8) (2022) 083801.
- [103] A. Pandey, J. Gigax, R. Pokharel, Machine learning interatomic potential for high-throughput screening of high-entropy alloys, *JOM* 74 (8) (2022) 2908–2920.
- [104] A. Stukowski, Visualization and analysis of atomistic simulation data with ovito—the open visualization tool, *Modelling and simulation in materials science and engineering* 18 (1) (2009) 015012.
- [105] S. Zhao, T. Egami, G. M. Stocks, Y. Zhang, Effect of d electrons on defect properties in equiatomic nicocr and nicofecr concentrated solid solution alloys, *Physical Review Materials* 2 (1) (2018) 013602.
- [106] M. Čák, T. Hammerschmidt, J. Rogal, V. Vitek, R. Drautz, Analytic bond-order po-

- tentials for the bcc refractory metals nb, ta, mo and w, *Journal of Physics: Condensed Matter* 26 (19) (2014) 195501.
- [107] S. Han, L. A. Zepeda-Ruiz, G. J. Ackland, R. Car, D. J. Srolovitz, Self-interstitials in v and mo, *Physical Review B* 66 (22) (2002) 220101.
- [108] L. Yang, P. Söderlind, J. A. Moriarty, Accurate atomistic simulation of $(a/2)_i$ 111 $_i$ screw dislocations and other defects in bcc tantalum, *Philosophical Magazine A* 81 (5) (2001) 1355–1385.
- [109] L. Ventelon, F. Willaime, C.-C. Fu, M. Heran, I. Ginoux, Ab initio investigation of radiation defects in tungsten: Structure of self-interstitials and specificity of di-vacancies compared to other bcc transition metals, *Journal of Nuclear Materials* 425 (1-3) (2012) 16–21.
- [110] M. Guinan, R. Stuart, R. Borg, Fully dynamic computer simulation of self-interstitial diffusion in tungsten, *Physical Review B* 15 (2) (1977) 699.
- [111] R. Pasianot, A. Monti, G. Simonelli, E. Savino, Computer simulation of sia migration in bcc and hcp metals, *Journal of nuclear materials* 276 (1-3) (2000) 230–234.
- [112] G. Nandipati, W. Setyawan, K. J. Roche, R. J. Kurtz, B. D. Wirth, Effect of confinement of sia cluster diffusion by impurities on radiation defect accumulation due to 14 mev neutrons in tungsten, *Journal of Nuclear Materials* 542 (2020) 152402.
- [113] S. Bukkuru, U. Bhardwaj, K. S. Rao, A. Rao, M. Warriar, M. Valsakumar, Kinetics of self-interstitial migration in bcc and fcc transition metals, *Materials Research Express* 5 (3) (2018) 035513.
- [114] K. Morishita, T. D. de la Rubia, A. Kimura, Mobility of self-interstitial atom clusters in vanadium, tantalum and copper, *Nuclear Instruments and Methods in Physics*

- Research Section B: Beam Interactions with Materials and Atoms 180 (1-4) (2001) 66–71.
- [115] W. Zhou, C. Zhang, Y. Li, Z. Zeng, Transport, dissociation and rotation of small self-interstitial atom clusters in tungsten, *Journal of Nuclear Materials* 453 (1) (2014) 202–209.
- [116] J. Wang, Q. Hou, B. Zhang, Migration behavior of self-interstitial defects in tungsten and iron, *Solid State Communications* 325 (2021) 114158.
- [117] T. D. Swinburne, P.-W. Ma, S. L. Dudarev, Low temperature diffusivity of self-interstitial defects in tungsten, *New Journal of Physics* 19 (7) (2017) 073024.
- [118] Y. Osetsky, A. V. Barashev, L. K. Béland, Z. Yao, K. Ferasat, Y. Zhang, Tunable chemical complexity to control atomic diffusion in alloys, *npj Computational Materials* 6 (1) (2020) 38.
- [119] T. Shi, Z. Su, J. Li, C. Liu, J. Yang, X. He, D. Yun, Q. Peng, C. Lu, Distinct point defect behaviours in body-centered cubic medium-entropy alloy nbzrti induced by severe lattice distortion, *Acta Materialia* 229 (2022) 117806.
- [120] Y. Li, W. Qiang, Defect properties of a body-centered cubic equiatomic tivzrta high-entropy alloy from atomistic simulations, *Journal of Physics: Condensed Matter* 35 (34) (2023) 345701.
- [121] V. Dubinko, S. Hu, Y. Li, C. Henager Jr, R. J. Kurtz, Dislocation vs. production bias revisited with account of radiation-induced emission bias. i. void swelling under electron and light ion irradiation, *Philosophical Magazine* 92 (33) (2012) 4113–4150.
- [122] W. Wolfer, The dislocation bias, *Journal of Computer-Aided Materials Design* 14 (2007) 403–417.

- [123] S. Golubov, B. Singh, H. Trinkaus, Defect accumulation in fcc and bcc metals and alloys under cascade damage conditions—towards a generalisation of the production bias model, *Journal of Nuclear Materials* 276 (1-3) (2000) 78–89.
- [124] C. Woo, B. Singh, Production bias due to clustering of point defects in irradiation-induced cascades, *Philosophical Magazine A* 65 (4) (1992) 889–912.
- [125] P. A. Olsson, Semi-empirical atomistic study of point defect properties in bcc transition metals, *Computational materials science* 47 (1) (2009) 135–145.
- [126] G. Ackland, R. Thetford, An improved n-body semi-empirical model for body-centred cubic transition metals, *Philosophical Magazine A* 56 (1) (1987) 15–30.
- [127] W. Xu, J. A. Moriarty, Atomistic simulation of ideal shear strength, point defects, and screw dislocations in bcc transition metals: Mo as a prototype, *Physical Review B* 54 (10) (1996) 6941.
- [128] K. Vörtler, C. Björkas, D. Terentyev, L. Malerba, K. Nordlund, The effect of cr concentration on radiation damage in fe–cr alloys, *Journal of Nuclear Materials* 382 (1) (2008) 24–30.
- [129] Y. Zhang, D. Schwen, X.-M. Bai, Effects of solute-sia binding energy on defect production behaviors in fe-based alloys, *Journal of Nuclear Materials* 509 (2018) 124–133.
- [130] D. Terentyev, P. Olsson, T. Klaver, L. Malerba, On the migration and trapping of single self-interstitial atoms in dilute and concentrated fe–cr alloys: Atomistic study and comparison with resistivity recovery experiments, *Computational Materials Science* 43 (4) (2008) 1183–1192.
- [131] A. Tunde Raji, S. Scandolo, R. Mazzarello, S. Nsengiyumva, M. Härting, D. Thomas Britton, Ab initio pseudopotential study of vacancies and self-interstitials in hcp titanium, *Philosophical Magazine* 89 (20) (2009) 1629–1645.

- [132] F. Willaime, Ab initio study of self-interstitials in hcp-zr, *Journal of nuclear materials* 323 (2-3) (2003) 205–212.
- [133] M. Ganchenkova, P. Vladimirov, V. Borodin, Vacancies, interstitials and gas atoms in beryllium, *Journal of Nuclear Materials* 386 (2009) 79–81.
- [134] C. Lu, L. Niu, N. Chen, K. Jin, T. Yang, P. Xiu, Y. Zhang, F. Gao, H. Bei, S. Shi, et al., Enhancing radiation tolerance by controlling defect mobility and migration pathways in multicomponent single-phase alloys, *Nature communications* 7 (1) (2016) 13564.
- [135] Z. H. Aitken, V. Sorkin, Y.-W. Zhang, Atomistic modeling of nanoscale plasticity in high-entropy alloys, *Journal of Materials Research* 34 (9) (2019) 1509–1532.
- [136] X. Zhou, S. He, J. Marian, Vacancy energetics and diffusivities in the equiatomic multielement nb-mo-ta-w alloy, *Materials* 15 (15) (2022) 5468.
- [137] J. Horak, T. Blewitt, Isochronal recovery of fast neutron irradiated metals, *Journal of Nuclear Materials* 49 (2) (1973) 161–180.
- [138] K. Wilson, M. Baskes, D. Seidman, An in situ field-ion microscope study of the recovery behavior of ion-irradiated tungsten and tungsten alloys, *Acta metallurgica* 28 (1) (1980) 89–102.
- [139] C. Parkin, M. Moorehead, M. Elbakhshwan, J. Hu, W.-Y. Chen, M. Li, L. He, K. Sridharan, A. Couet, In situ microstructural evolution in face-centered and body-centered cubic complex concentrated solid-solution alloys under heavy ion irradiation, *Acta Materialia* 198 (2020) 85–99.
- [140] J. Zhou, M. Kirk, P. Baldo, S. Guo, F. Lu, Phase stability of novel hfnbtativzr refractory high entropy alloy under ion irradiation, *Materials Letters* 305 (2021) 130789.
- [141] O. El Atwani, H. Vo, M. Tunes, C. Lee, A. Alvarado, N. Krienke, J. Poplawsky, A. Kohnert, J. Gigax, W.-Y. Chen, et al., A quinary wtacrvhf nanocrystalline refrac-

- tory high-entropy alloy withholding extreme irradiation environments, *nature communications* 14 (1) (2023) 2516.
- [142] F. Maresca, W. A. Curtin, Theory of screw dislocation strengthening in random bcc alloys from dilute to “high-entropy” alloys, *Acta Materialia* 182 (2020) 144–162.
- [143] F. Maresca, W. A. Curtin, Mechanistic origin of high strength in refractory bcc high entropy alloys up to 1900k, *Acta Materialia* 182 (2020) 235–249.
- [144] B. Yin, W. Curtin, Origin of high strength in the cocrfenipd high-entropy alloy, *Materials Research Letters* 8 (6) (2020) 209–215.
- [145] A. Ghafarollahi, F. Maresca, W. Curtin, Solute/screw dislocation interaction energy parameter for strengthening in bcc dilute to high entropy alloys, *Modelling and Simulation in Materials Science and Engineering* 27 (8) (2019) 085011.
- [146] X. Wang, F. Maresca, P. Cao, The hierarchical energy landscape of screw dislocation motion in refractory high-entropy alloys, *Acta Materialia* 234 (2022) 118022.
- [147] S. Rao, C. Woodward, B. Akdim, O. Senkov, A model for interstitial solid solution strengthening of body centered cubic metals, *Materialia* 9 (2020) 100611.
- [148] S. Rao, E. Antillon, C. Woodward, B. Akdim, T. Parthasarathy, O. Senkov, Solution hardening in body-centered cubic quaternary alloys interpreted using suzuki’s kink-solute interaction model, *Scripta Materialia* 165 (2019) 103–106.
- [149] W. Curtin, S. Rao, C. Woodward, Progress and challenges in the theory and modeling of complex concentrated alloys, *Mrs Bulletin* 47 (2) (2022) 151–157.
- [150] S. Rao, C. Woodward, B. Akdim, O. Senkov, D. Miracle, Theory of solid solution strengthening of bcc chemically complex alloys, *Acta Materialia* 209 (2021) 116758.

- [151] R. Feng, B. Feng, M. C. Gao, C. Zhang, J. C. Neuefeind, J. D. Poplawsky, Y. Ren, K. An, M. Widom, P. K. Liaw, Superior high-temperature strength in a supersaturated refractory high-entropy alloy, *Advanced Materials* 33 (48) (2021) 2102401.
- [152] H. Zhang, Y. Zhao, J. Cai, S. Ji, J. Geng, X. Sun, D. Li, High-strength nbmotax refractory high-entropy alloy with low stacking fault energy eutectic phase via laser additive manufacturing, *Materials & Design* 201 (2021) 109462.
- [153] A. Stukowski, D. Cereceda, T. D. Swinburne, J. Marian, Thermally-activated non-schmid glide of screw dislocations in w using atomistically-informed kinetic monte carlo simulations, *International Journal of Plasticity* 65 (2015) 108–130.
- [154] Y. Zhao, J. Marian, Direct prediction of the solute softening-to-hardening transition in w–re alloys using stochastic simulations of screw dislocation motion, *Modelling and Simulation in Materials Science and Engineering* 26 (4) (2018) 045002. doi: 10.1088/1361-651x/aaaecf.
URL <https://doi.org/10.1088/1361-651x/aaaecf>
- [155] Y. Zhao, L. Dezerald, M. Pozuelo, X. Zhou, J. Marian, Simulating the mechanisms of serrated flow in interstitial alloys with atomic resolution over diffusive timescales, *Nature Communications* 11 (1) (2020) 1–8.
- [156] X. Zhou, S. He, J. Marian, Cross-kinks control screw dislocation strength in equiatomic bcc refractory alloys, *Acta Materialia* 211 (2021) 116875.
- [157] W. Cai, A. Arsenlis, C. R. Weinberger, V. V. Bulatov, A non-singular continuum theory of dislocations, *Journal of the Mechanics and Physics of Solids* 54 (3) (2006) 561 – 587. doi:<https://doi.org/10.1016/j.jmps.2005.09.005>.
URL <http://www.sciencedirect.com/science/article/pii/S002250960500195X>
- [158] A. Stukowski, D. Cereceda, T. D. Swinburne, J. Marian, Thermally-activated non-schmid glide of screw dislocations in w using atomistically-informed kinetic monte

- carlo simulations, *International Journal of Plasticity* 65 (2015) 108 – 130. doi:<https://doi.org/10.1016/j.ijplas.2014.08.015>.
URL <http://www.sciencedirect.com/science/article/pii/S074964191400182X>
- [159] S. He, E. Overly, V. Bulatov, J. Marian, D. Cereceda, Coupling 2d atomistic information to 3d kink-pair enthalpy models of screw dislocations in bcc metals, *Physical Review Materials* 3 (10) (2019) 103603.
- [160] S. Rao, C. Varvenne, C. Woodward, T. Parthasarathy, D. Miracle, O. Senkov, W. Curtin, Atomistic simulations of dislocations in a model bcc multicomponent concentrated solid solution alloy, *Acta Materialia* 125 (2017) 311–320.
- [161] S. Rao, C. Woodward, B. Akdim, E. Antillon, T. Parthasarathy, O. Senkov, Estimation of diffusional effects on solution hardening at high temperatures in single phase compositionally complex body centered cubic alloys, *Scripta Materialia* 172 (2019) 135–137.
- [162] B. Chen, S. Li, H. Zong, X. Ding, J. Sun, E. Ma, Unusual activated processes controlling dislocation motion in body-centered-cubic high-entropy alloys, *Proceedings of the National Academy of Sciences* 117 (28) (2020) 16199–16206.
- [163] E. Rodary, D. Rodney, L. Proville, Y. Bréchet, G. Martin, Dislocation glide in model ni (al) solid solutions by molecular dynamics, *Physical Review B* 70 (5) (2004) 054111.
- [164] J. Marian, A. Caro, Moving dislocations in disordered alloys: Connecting continuum and discrete models with atomistic simulations, *Physical Review B* 74 (2) (2006) 024113.
- [165] A. Ghafarollahi, W. A. Curtin, Theory of double-kink nucleation in dilute bcc alloys, *Acta Materialia* 196 (2020) 635–650.

- [166] X. Zhou, X. Wang, L. Fey, S. He, I. Beyerlein, P. Cao, J. Marian, Models of dislocation glide and strengthening mechanisms in bcc complex concentrated alloys, *MRS Bulletin* (2023) 1–13.
- [167] J. Marian, W. Cai, V. V. Bulatov, Dynamic transitions from smooth to rough to twinning in dislocation motion, *Nature materials* 3 (3) (2004) 158.
- [168] Y. Bu, Y. Wu, Z. Lei, X. Yuan, H. Wu, X. Feng, J. Liu, J. Ding, Y. Lu, H. Wang, et al., Local chemical fluctuation mediated ductility in body-centered-cubic high-entropy alloys, *Materials Today* 46 (2021) 28–34.
- [169] J. Wang, R. G. Hoagland, A. Misra, Room-temperature dislocation climb in metallic interfaces, *Applied Physics Letters* 94 (13) (2009) 131910.
- [170] M. Pozuelo, J. Marian, Microscale deformation controlled by compositional fluctuations in equiatomic nb–mo–ta–w alloys, *Materials Science and Engineering: A* 856 (2022) 143892.
- [171] M. Gilbert, S. Queyreau, J. Marian, Stress and temperature dependence of screw dislocation mobility in α -fe by molecular dynamics, *Physical Review B* 84 (17) (2011) 174103.
- [172] J. Chaussidon, M. Fivel, D. Rodney, The glide of screw dislocations in bcc fe: atomistic static and dynamic simulations, *Acta materialia* 54 (13) (2006) 3407–3416.
- [173] Y. Fan, Y. N. Osetskiy, S. Yip, B. Yildiz, Mapping strain rate dependence of dislocation-defect interactions by atomistic simulations, *Proceedings of the National Academy of Sciences* 110 (44) (2013) 17756–17761.
- [174] J.-P. Couzini, L. Lilensten, Y. Champion, G. Dirras, L. Perrière, I. Guillot, On the room temperature deformation mechanisms of a tizrhnbtarefractory high-entropy alloy, *Materials Science and Engineering: A* 645 (2015) 255 – 263. doi:

<https://doi.org/10.1016/j.msea.2015.08.024>.

URL <http://www.sciencedirect.com/science/article/pii/S0921509315302720>

- [175] C. Lee, F. Maresca, R. Feng, Y. Chou, T. Ungar, M. Widom, K. An, J. D. Poplawsky, Y.-C. Chou, P. K. Liaw, et al., Strength can be controlled by edge dislocations in refractory high-entropy alloys, *Nature communications* 12 (1) (2021) 1–8.
- [176] R. Kubilay, A. Ghafarollahi, F. Maresca, W. Curtin, High energy barriers for edge dislocation motion in body-centered cubic high entropy alloys, *Npj computational materials* 7 (1) (2021) 112.
- [177] K.-K. Tseng, H.-H. Huang, W.-R. Wang, J.-W. Yeh, C.-W. Tsai, Edge-dislocation-induced ultrahigh elevated-temperature strength of hfmombtaw refractory high-entropy alloys, *Science and Technology of Advanced Materials* 23 (1) (2022) 642–654.
- [178] S. He, X. Zhou, D. Mordehai, J. Marian, Thermal super-jogs control the high-temperature strength plateau in nb-mo-ta-w alloys, *Acta Materialia* 244 (2023) 118539.